Earth and Space Science

Correspondence to:
B. V. Wogsland,
bwogsla1@vols.utk.edu

Science and Science-Enabling Activities of the SHERLOC and WATSON Imaging Systems in Jezero Crater, Mars

B. V. Wogsland[1] , M. E. Minitti[2] , L. C. Kah[1] , R. A. Yingst[3] , W. Abbey[4,†] , R. Bhartia[5], L. Beegle[6], B. L. Bleefeld[7], E. L. Cardarelli[4] , P. G. Conrad[8], K. Edgett[6] , K. Hickman-Lewis[9], J. Hugget[7] , S. Imbeah[7], M. R. Kennedy[7] , C. Lee[10], B. E. Nixon[7], J. I. Núñez[11] , A. Pascuzzo[7], M. Robinson[4], C. Rodriguez Sanchez-Vahamonde[7] , E. Scheller[12], S. Sharma[4], S. Siljeström[13] , K. Steadman[4] , K. Winchell[7], and Michael A. Ravine[7]

[1]University of Tennessee, Knoxville, MD, USA, [2]Framework, Silver Spring, MD, USA, [3]Planetary Science Institute, San Diego, CA, USA, [4]Jet Propulsion Laboratory, California Institute of Technology, Pasadena, CA, USA, [5]Photon Systems Incorporated, Covina, CA, USA, [6]Formerly with NASA Jet Propulsion Laboratory, California Institute of Technology, Pasadena, CA, USA, [7]Malin Space Science Systems, San Diego, CA, USA, [8]Carnegie Institution for Science, Washington, DC, USA, [9]The Natural History Museum, Università di Bologna, Bologna, Italy, [10]NASA Johnson Space Center, Houston, TX, USA, [11]Johns Hopkins University Applied Physics Laboratory, Laurel, MD, USA, [12]Massachusetts Institute of Technology, Cambridge, MA, USA, [13]RISE Research Institutes of Sweden, Stockholm, Sweden

Abstract During its first year of operation, the Perseverance rover explored the cratered and fractured floor of Jezero crater on Mars. Here, we report the use of the Scanning Habitability Environments with Raman and Luminescence for Organics and Chemicals (SHERLOC) imaging system that includes two high-resolution cameras, the Autofocus and Contextual Imager (ACI) and Wide Angle Topographic Sensor for Operations and eNgineering (WATSON). ACI is a fixed focus gray scale imager with a resolution of 10.1 µm/pixel whereas WATSON is a variable field of view, variable focus imager capable of resolution down to 14 µm/pixel. WATSON is a reflight of the MArs Hand Lens Imager (MAHLI) imager and has similar capabilities. During first-time activities, WATSON was used to support both science and engineering operations related to sample and abrasion patch assessment and sample collection and caching. WATSON also documented the deployment of the Ingenuity helicopter. The Crater Floor Campaign identified two primary rock units, the Máaz formation and the Séítah formation, which have been interpreted as lava flows and an olivine cumulate, respectively. Interpretation of rock textures with WATSON and ACI images was limited to abraded surfaces because unmodified outcrop surfaces (herein termed "natural surfaces") show high degrees of dust covering, wind abrasion, and coating by secondary mineral products. WATSON and ACI images support the hypothesis that the material of both the Máaz and Séítah formations consists of largely aqueously altered mafic materials with varying igneous origins.

Plain Language Summary The SHERLOC imaging system has been used for a variety of tasks during the first year of operations as part of the Perseverance rover's mission to Jezero Crater. It has been used during scientific observations to understand textures documenting the aqueous alteration history of the crater. It has also been used to support operations by documenting the deployment of the Ingenuity helicopter and the utilization of the sampling and caching hardware.

1. Introduction

One of the primary goals of NASA is the search for life elsewhere in the galaxy, with the planet Mars being key in reaching this goal. Available geologic evidence suggests that, early in the history of Mars, the planet had extended periods of liquid water activity at its surface including standing bodies of water and a hydrological cycle similar to that on the Earth (Andrews-Hanna & Lewis, 2011; Salese et al., 2019). These liquid water environments existed on Mars at roughly the same time that life originated on the Earth and likely had chemical compositions that are considered habitable (e.g., Carr & Head, 2003; Grotzinger et al., 2014; Perron et al., 2007). The Martian surface geologic record includes sedimentary sequences documenting aqueous environments that existed from the Noachian to Hesperian periods (from 4.1 to 3.0 billion years ago; e.g., Edgett & Sarkar, 2021; Fassett & Head, 2005; Malin & Edgett, 2003; Salese et al., 2020). Nearly a dozen different types of aqueous systems have been identified from these periods, including alluvial, fluvial, lacustrine, and deltaic environments, and

Data curation: W. Abbey, R. Bhartia, B. L. Bleefeld, E. L. Cardarelli, P. G. Conrad, K. Edgett, J. Hugget, S. Imbeah, M. R. Kennedy, C. Lee, B. E. Nixon, A. Pascuzzo, M. Robinson, C. Rodriguez Sanchez-Vahamonde, E. Scheller, S. Sharma, K. Steadman
Formal analysis: B. V. Wogsland, M. E. Minitti, L. C. Kah, R. A. Yingst, P. G. Conrad, K. Edgett
Funding acquisition: L. C. Kah, R. Bhartia, L. Beegle
Methodology: L. C. Kah, R. A. Yingst, W. Abbey, K. Edgett, M. R. Kennedy
Project Administration: R. Bhartia, L. Beegle
Resources: R. Bhartia, M. R. Kennedy
Software: W. Abbey, B. L. Bleefeld, K. Edgett, M. R. Kennedy
Supervision: M. E. Minitti, L. C. Kah, R. A. Yingst, R. Bhartia, L. Beegle
Validation: M. E. Minitti, L. C. Kah, R. A. Yingst, E. L. Cardarelli, P. G. Conrad, K. Edgett, M. R. Kennedy, J. I. Núñez, S. Siljeström
Visualization: L. C. Kah, Michael A. Ravine
Writing – original draft: B. V. Wogsland, M. E. Minitti, L. C. Kah, R. A. Yingst, W. Abbey, R. Bhartia, L. Beegle, E. L. Cardarelli, P. G. Conrad, K. Edgett, M. Robinson, S. Sharma
Writing – review & editing: B. V. Wogsland, M. E. Minitti, L. C. Kah, R. A. Yingst, W. Abbey, R. Bhartia, L. Beegle, E. L. Cardarelli, P. G. Conrad, K. Hickman-Lewis, C. Lee, B. E. Nixon, J. I. Núñez, A. Pascuzzo, M. Robinson, E. Scheller, S. Sharma, S. Siljeström, K. Steadman, K. Winchell

evidence for hydrothermal fluid activity (Brown et al., 2010; Davis et al., 2016; Murchie et al., 2009; Williams et al., 2013). The Perseverance rover is the latest mission to explore the Martian surface and represents the first step in a multifaceted mission to identify geologically interesting and astrobiologically relevant samples that will be collected and cached. Pending Congressional approval, these samples will potentially be returned to Earth as part of the Mars Sample Return mission in the 2030s (Farley et al., 2020, 2022; Kminek et al., 2022; Moeller et al., 2021).

The Scanning Habitable Environments with Raman and Luminescence for Organics and Chemicals (SHERLOC) investigation is one of seven instruments that are a part of the payload of the Perseverance rover. It consists of a robotic arm-mounted instrument that acquires microscopic images of surface material, performs documentation imaging of the rover (including taking rover selfies, cf., Williford et al., 2018), and characterizes the spatial distribution of minerals and organic molecules via fluorescence and deep UV Raman spectroscopy (Bhartia et al., 2021). To accomplish these tasks, SHERLOC was designed with two distinct systems that provide high-resolution images and a contextual framework for analyses. The WATSON (Wide Angle Topographic Sensor for Operations and eNgineering) is a reflight of the MAHLI (MArs Hand Lens Imager) that is a part of the Curiosity rover (Edgett et al., 2012). WATSON obtains full-color images from microscopic scales (∼13 µm/pixel) to infinity and is used for initial textural analysis of rock and regolith targets, as well as to assess potential proximity science targets and the safety of robotic arm activities (Edgett et al., 2012). The ACI (Autofocus Contextual Imager) is a fixed field, 10.1 µm/pixel resolution grayscale imager used to obtain best-focus and colocate laser spots with surface feature analyzed during SHERLOC spectroscopic investigations (Bhartia et al., 2021). These imaging systems provide critical context for the SHERLOC investigation in documenting organic-mineral relationships within geologic units of the Jezero crater floor, including the presence of organic compounds related to carbonation of ultramafic minerals (Scheller et al., 2021), the precipitation of sulfate and perchlorate compounds from late-stage diagenetic brines (Corpolongo et al., 2023; Scheller et al., 2022) and the preservation of aromatic organic compounds associated with diagenetic fluid flow (Sharma et al., 2023).

2. The Mars 2020 Mission

The Perseverance rover mission is currently exploring Jezero crater (Figure 1), which sits on the western edge of the Isidis Basin between the Syrtis Major volcanic complex and the Nili Fossae region (Goudge et al., 2015; Mustard et al., 2007; Sun & Stack, 2020). Jezero was chosen as the highest-potential landing site for the Mars 2020 mission. Although critical fine-scale details of the geology were poorly constrained prior to the start of the Mars 2020 mission, the rover landing site on the Jezero crater floor had been identified from orbital spectroscopy as containing a diverse set of minerals that includes both olivine and pyroxene associated with emplacement of potential igneous lithologies (Brown et al., 2020; Goudge et al., 2015; Kremer et al., 2019; Mandon et al., 2020; Mustard et al., 2007, 2009), carbonate and silica phases suggesting postdepositional alteration of igneous mineralogies (Ehlmann et al., 2009; Horgan et al., 2020; Mandon et al., 2020; Mangold et al., 2007; Tarnas et al., 2019; Viviano et al., 2013), clay-rich phases associated with sedimentary deposition within a crater-wide lacustrine system (Goudge et al., 2015; Horgan et al., 2020), and carbonate-rich deposits associated with the Jezero lake-margin (Horgan et al., 2020; Zastrow & Glotch, 2021). The watershed region from which sedimentation within Jezero crater was derived is also geologically diverse and includes >3.8 Ga (pre-Isidis) basement (Goudge et al., 2015; Mangold et al., 2007; Mustard et al., 2007, 2009; Scheller & Ehlmann, 2020), a regional ∼3.8 Ga olivine-bearing unit (Mandon et al., 2020) that drapes the Jezero crater rim (Bramble et al., 2017; Kremer et al., 2019; Mandon et al., 2020), and a series of younger mafic units that are cross-cut by Jezero-related fluvial activity (Bramble et al., 2017; Goudge et al., 2015; Horgan et al., 2020; Hundal et al., 2022). Combined, such lithologies suggest the potential to collect a suite of samples that will ultimately help constrain regional chronology and that have high potential for the preservation of biosignatures associated with deltaic and lacustrine deposition, and postdepositional aqueous activity (Mangold et al., 2020, 2021; Salese et al., 2020; Tarnas et al., 2021).

The Perseverance rover landed in the western region of Jezero crater in February 2021. Immediately after landing, the rover and instruments teams commenced a commissioning phase followed by initial investigation of crater floor lithologies (Crater Floor Campaign; Sun et al., 2023). Geological units assessed during this campaign reflect materials mapped by Stack et al. (2020) as Crater Floor Fractured 1 (CF-F1), Crater Floor Fractured Rough (CF-Fr), and Undifferentiated Smooth (Us) (Figure 1b). Herein, rocks from CF-F1 are referred to as the Séítah formation and rocks from CF-Fr (the dark-toned floor unit of Shahrzad et al. (2019) or volcanic floor
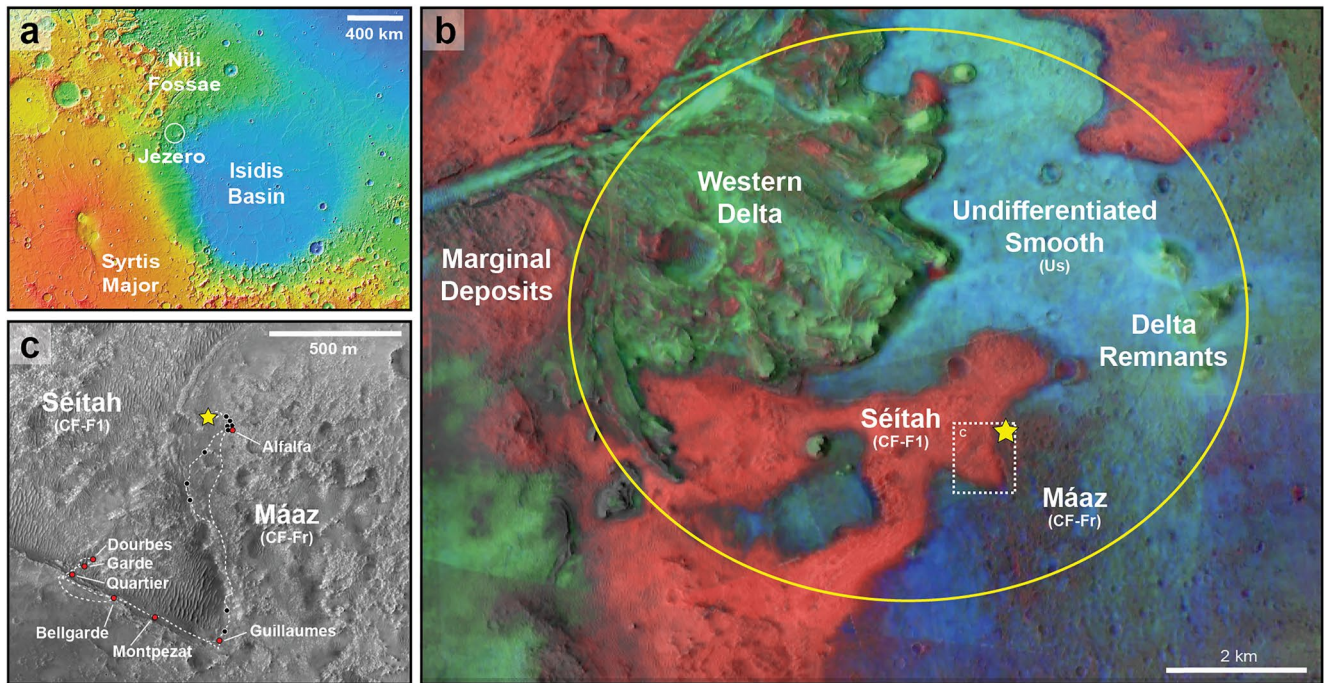
Figure 1. Regional setting of the Mars 2020 mission. (a) Jezero crater (18.9°N, 77.5°E) sits on the northwestern margin of Isidis basin. (b) Primary features of the crater floor in the region of the landing ellipse (see text for details). Yellow star marks Octavia E. Butler Landing. Location of c is the dotted rectangle. Background colors represent spectral signatures of mafic minerals as observed from orbit; red represents olivine, green represents low calcium pyroxene, and blue represents high calcium pyroxene (Horgan et al., 2020). (c) Detail showing the drive path of the Perseverance rover during the Crater Floor Campaign (dotted white line). Yellow star marks Octavia E. Butler Landing. Black circles represent positions where Wide Angle Topographic Sensor for Operations and eNgineering (WATSON) imaging was acquired; red circles mark abrasion patches on which both WATSON and Autofocus and Contextual Imager (ACI) images were acquired.

unit of Goudge et al. (2015)) are referred to as the Máaz formation; materials associated with Us are represented largely by regolith.

Rocks of the Séítah formation represent the stratigraphically lowest exposed materials of the Jezero crater floor. The Séítah formation comprises a series of eroded outcrops that are irregularly distributed across the crater floor at the margins of the dark-toned crater floor in regions dominated by sand dunes (Crumpler et al., 2023). Rocks of the Séítah formation show orbital and in situ detections of olivine and carbonate (Beyssac et al., 2023; Brown et al., 2020; Corpolongo et al., 2023; Liu et al., 2022; Rice et al., 2023; Wiens et al., 2022) that are similar to those observed within a regional olivine-carbonate unit that occurs across the Nili Fossae and Northeast Syrtis region (Brown et al., 2020; Kremer et al., 2019; Mandon et al., 2020; Scheller & Ehlmann, 2020), including within the Jezero crater watershed (Brown et al., 2020; Goudge et al., 2015; Horgan et al., 2020). The Máaz formation consists of a series of thinly layered, crater-retaining units that overlie, potentially with a significant unconformity, rocks of the Séítah formation and comprise the basis of the unit originally described as the dark-toned/volcanic floor unit (Holm-Alwmark et al., 2021; Stack et al., 2020). Orbital detections of the dark-toned floor unit show a variety of mafic lithologies, including detections of high-Ca pyroxene and sometimes olivine (Goudge et al., 2015; Horgan et al., 2020; Hundal et al., 2022), with mixed olivine-pyroxene detections correlating to regions that have higher thermal inertia (Horgan et al., 2020) and evidence for exposed outcrops. By contrast, regions of the dark-toned floor unit that are dominated by pyroxene detections correlate with regions of distinctly lower thermal inertia (Horgan et al., 2020), here associated with regolith mapped as Us. One of the key goals of the Crater Floor Campaign (Sun et al., 2023) was to determine the origin and emplacement of these key crater floor units.

3. WATSON and ACI Imaging Systems

The WATSON and ACI imaging systems are part of the broader SHERLOC instrument package (Bhartia et al., 2021). Both imaging systems (lenses and charge-coupled devices) are integrated within the SHERLOC instrument and mounted on a rotating turret at the end of the Perseverance rover robotic arm (Figure 2). The two cameras,
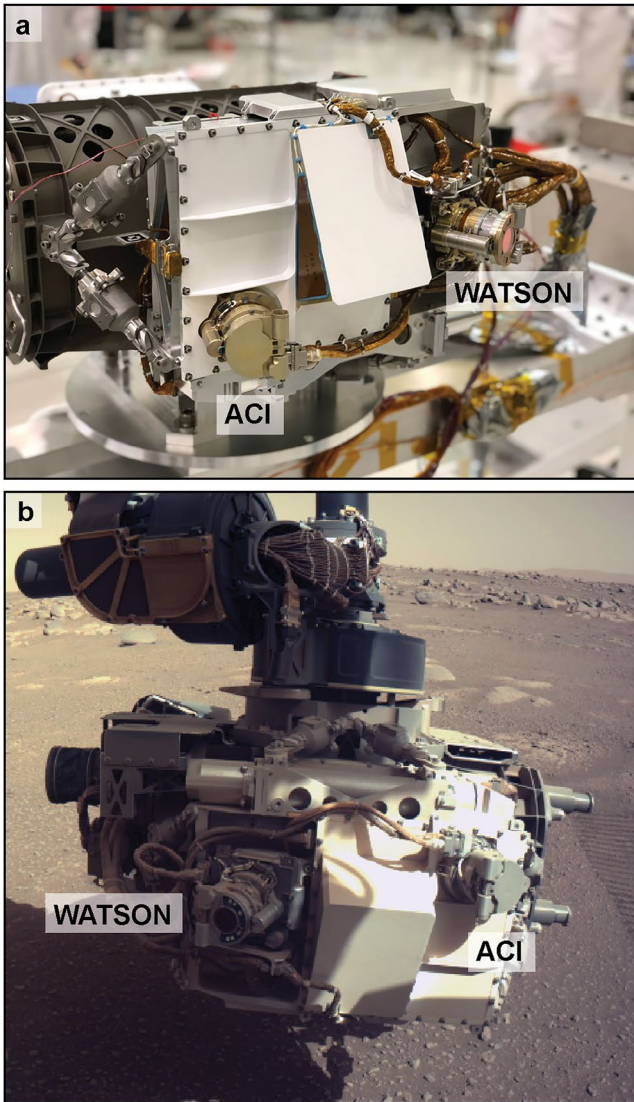
Figure 2. Scanning Habitability Environments with Raman and Luminescence for Organics and Chemicals (SHERLOC) Turret Assembly (STA) unit. (a) STA viewed prelaunch, showing both Wide Angle Topographic Sensor for Operations and eNgineering (WATSON) and Autofocus and Contextual Imager (ACI) camera heads (Bhartia et al., 2021). A transparent dust cover permits WATSON to be used with or without the dust cover in place. Both imagers have a suite of LEDs to enable use under a wide range of lighting conditions. (b) Image of STA taken on Sol 30 during instrument check-out. Image FLF_0030_0669613118_371FDR_N0030828FHAZ00201_0A0295J01.

however, are not coboresighted, and require that the robotic arm and turret be repositioned for each imager before analyzing a chosen geological target. WATSON, a reflight of MAHLI, was designed for the high-resolution optical investigation of geologic materials when using the robotic arm for proximity science activities (Bhartia et al., 2021; Edgett et al., 2012; Kah et al., 2018; Minitti et al., 2013; Yingst, Edgett, et al., 2016). This camera consists of a 1,200 × 1,600-pixel charge-coupled device (CCD) with a macro-lens capable of focusing from approximately 2 cm to infinity; color is produced by red-green-blue microfilters arranged on the CCD in a Bayer pattern (Bhartia et al., 2021; Edgett et al., 2012, 2019). Typical high-spatial resolution imaging on Mars using WATSON involves placing the camera at working distances (i.e., the distance between the front lens and the image target) of approximately 2.5–40.0 cm, which provides an image resolution from ~13 to 150 μm/pixel and a field of view that ranges from 1.7 × 2.3 cm to 18 × 24 cm.

Like its predecessor instrument (cf., Yingst, Cropper, et al., 2016; Yingst, Edgett, et al., 2016), the position of WATSON on the robotic arm and its ability to focus over a wide range of working distances—including focusing at infinity (Figure 3)—combine to provide an ideal instrument for science and for supporting engineering activities. WATSON can be positioned to image rover hardware, acquire mosaics showing the rover within the Martian landscape (i.e., selfies; Figure 3c), and even image features in the sky. WATSON can also image a variety of instrument calibration targets and is therefore critical to instrument calibration activities (Fries et al., 2022).

By contrast, ACI was designed to provide context views for SHERLOC's spectroscopic measurements and to focus SHERLOC's 248.6 nm deep-ultraviolet laser (Bhartia et al., 2021). The design of the ACI takes advantage of the proven success of the MAHLI instrument to integrate heritage hardware and software elements to permit acquisition of grayscale images on a 1,200 × 1,600-pixel CCD. In-focus ACI images are obtained at working distances of ~4.8 ± 0.835 cm, which provides an image resolution of 10.1 μm/pixel. The grayscale ACI provides sharper focus for the deep-UV laser than could be achieved using a Bayer pattern CCD.

3.1. Image Acquisition

WATSON and ACI images can be acquired by both manual and autofocusing via a step motor; focus position is expressed as a motor count and is used to calculate both working distance and pixel scale (Bhartia et al., 2021; Edgett, 2021; Edgett et al., 2012). Manual focus is performed by commanding the camera to move the lens to a specific motor count position; autofocus is achieved by commanding the camera to step through several focus positions while imaging a subframed portion of the target to establish the best-focus motor count (Edgett et al., 2012).

During normal operations multiple images are usually acquired by both WATSON or ACI, particularly at working distances of 6 cm or less. A typical WATSON observation at these close working distances includes 10 images: a 480 × 480-pixel autofocus subframe at the center of the CCD to focus the camera, a full-frame view of the target, and an 8-image focus stack that can be merged to provide a best-focus image. Acquisition of just two images (autofocus subframe and full-frame) is more common at larger working distances when the WATSON depth of field can effectively capture target topography in focus. Acquisition of additional images (e.g., a second full-frame with a different exposure duration, a 16-image focus stack) provides assurance of a high-quality image product even under challenging lighting or focus conditions. WATSON mosaic and stereo image acquisition (cf., Yingst, Edgett, et al., 2016) requires movement of the robotic arm between successive images. As an alternative to qualitative stereo images, quantitative relief models can be generated using additional overlapping WATSON images and can produce
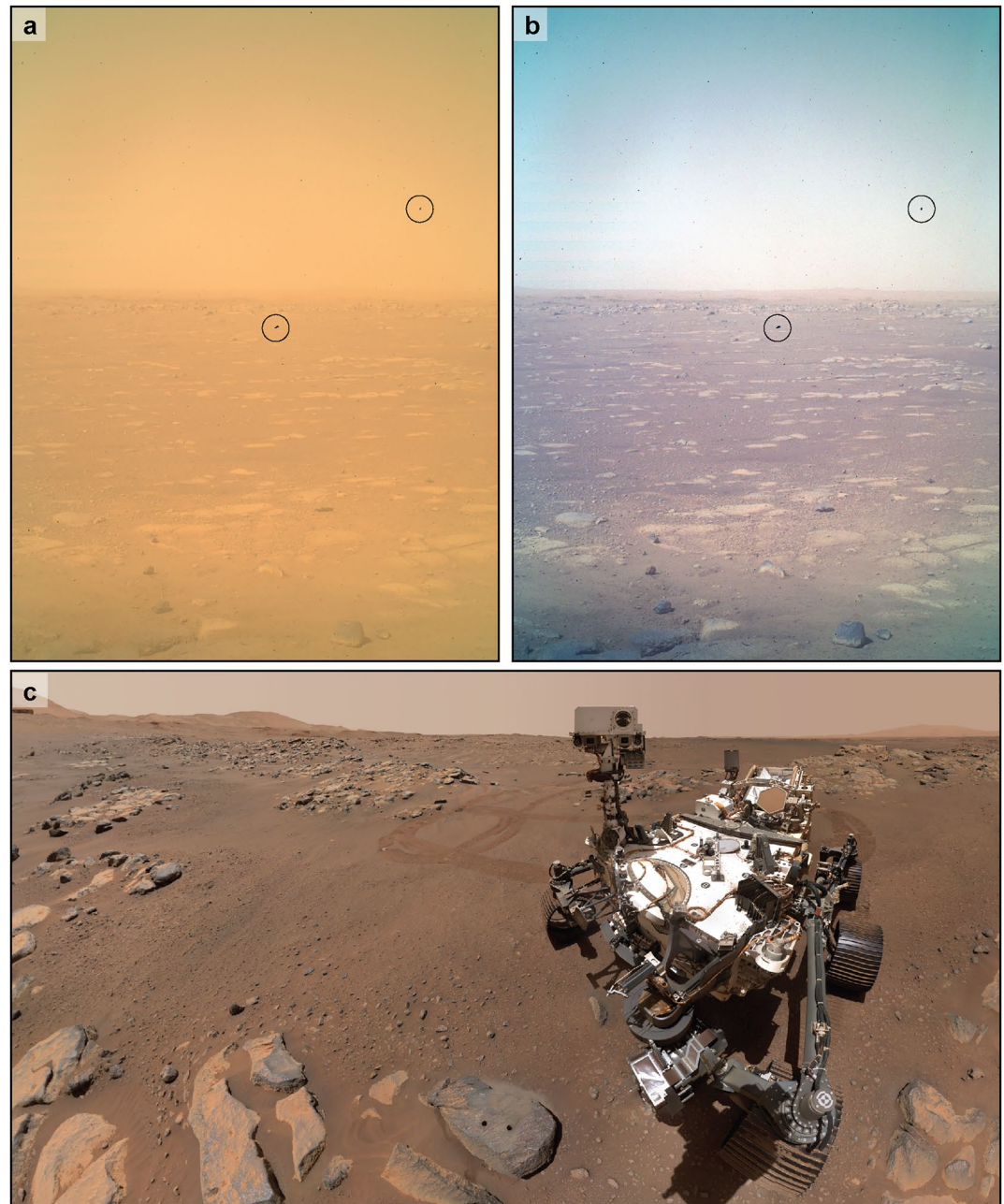
Figure 3. Noteworthy first images from Wide Angle Topographic Sensor for Operations and eNgineering (WATSON) after landing of the Perseverance rover. (a) Sol 11 image taken by WATSON with dust cover closed. Orange hue results from dust lofted during the landing event that adhered to the dust cover. Prominent dark specks (circled) result from prelaunch debris on the CCD and are removed in other WATSON images via masking or interpolation. (b) Color-corrected version of the image, with focus at infinity. Image SIF_0011_0667926298_145FDR_N0030000SRLC08000_0000LMJ01. (c) Perseverance selfie after first two core samples at "Rochette" showing the two drill holes left by sampling activities. The abraded target is obscured by drill tailings NASA/JPL-Caltech/MSSS.

topographic measurements at submillimeter scales (Garvin et al., 2017). The ACI camera uses a similar acquisition pathway, with 256×256 pixel autofocus subframes followed by up to 31 full-frame images in a focus stack. Additionally, ACI can utilize a gimbaled mirror within the SHERLOC Turret Assembly unit to acquire an ACI image mosaic without additional movement of the robotic arm (Bhartia et al., 2021).

WATSON and ACI can use natural or LED illumination during image acquisition. Both imagers have two groups of two white light LEDs and one group of two 365 nm long wavelength UV LEDs that can be commanded
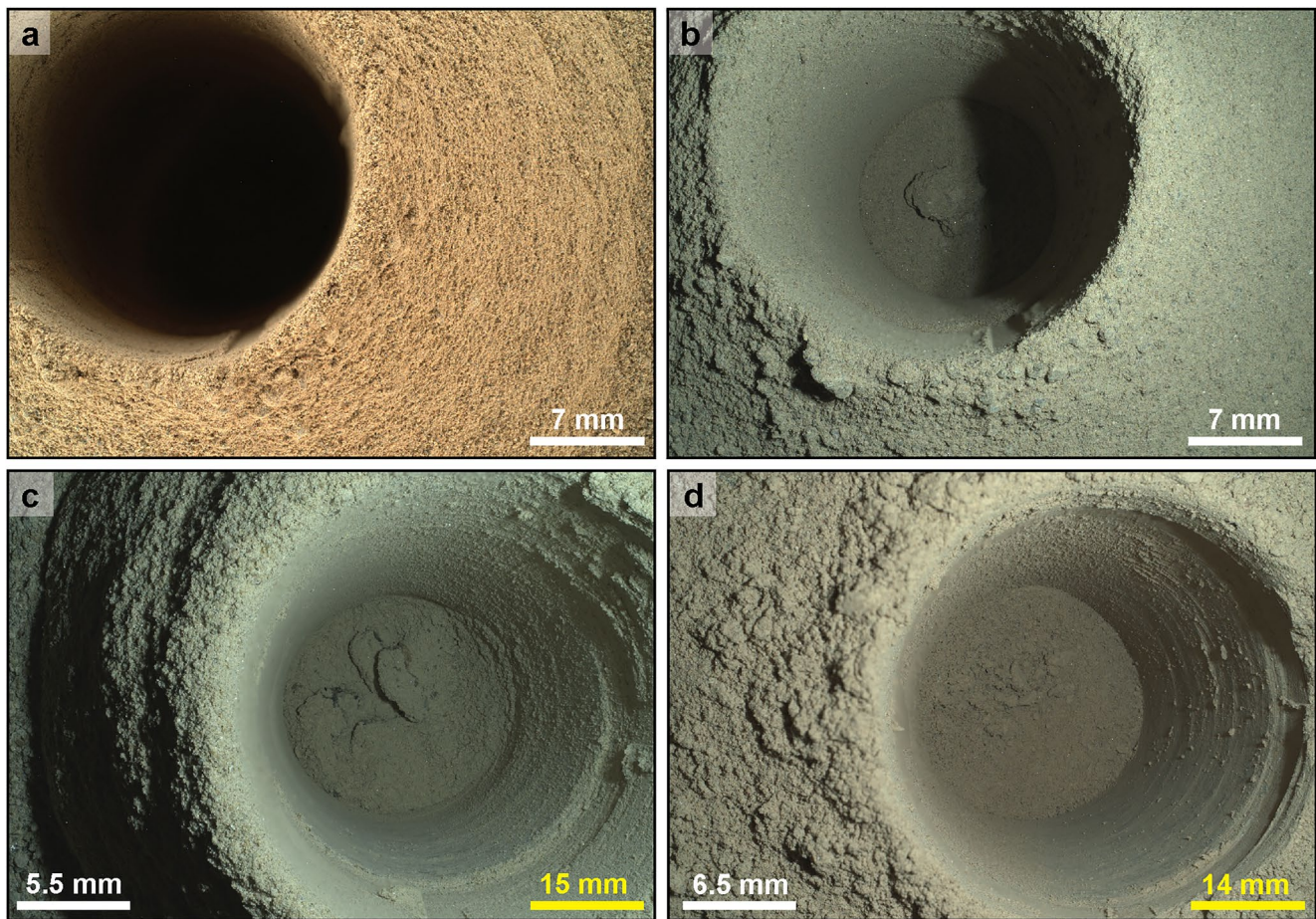
Figure 4. Wide Angle Topographic Sensor for Operations and eNgineering (WATSON) Images down borehole. These images exemplify self-shadowed and well illuminated images down sampling boreholes. (a) A daytime failed borehole image of Roubion is self-shadowed and the bottom of the hole is not visible. Image: SI1_0199_0684601302_753ECZ_N0070000SRLC00058_000095J01. (b) This nighttime focus merge of Roubion borehole is still self-shadowed because WATSON is not lined up correctly and the LED illumination masks the bottom of the hole. (c) This 6.3 cm stand-off focus merge of the Salette borehole (Brac outcrop, Séítah) was acquired at night using white LEDs. (d) Within Máaz, this 6 cm stand-off focus merge of the Hahonih borehole from the Ch'ał sample location. In c and d, White scale bar references the top of the borehole and yellow scale bore references the bottom.

separately or simultaneously to provide optimal lighting conditions (Bhartia et al., 2021; Edgett et al., 2012). Based on experience with MAHLI (cf., Edgett et al., 2015; Yingst, Cropper, et al., 2016; Yingst, Edgett, et al., 2016), the preferred illumination for WATSON and ACI imaging is under full sun; partially shadowed conditions are challenging in terms of image exposure. Full sun conditions are typically achieved at low incidence angles of illumination, as the sun must be low enough in the sky for light to make it in between the turret and the target (e.g., Figure 2b). At lower incidence angles, the lighting also better accentuates surface relief. Diffuse illumination from full shadow conditions can make surface relief more challenging to discern. Full sun illumination also reveals the natural colors of the target under Martian conditions, whereas diffuse illumination from full shadow conditions imparts an orange hue to target images.

LEDs associated with WATSON and ACI are most often used for nighttime imaging (cf., Minitti et al., 2014). WATSON imaging at night with white LEDs minimizes effects of shadowing—particularly self-shadowing when imaging down a borehole (Figure 4). During nighttime operation, using both sets of white LEDs together reduces shadows cast by target topography, while imaging with one group of white LEDs, then the other, provides the opportunity to examine detailed surface relief under discrete lighting conditions. White LED illumination during nighttime imaging yields the closest approximation to true color, allowing better comparison of color images across localities. UV LED illumination permits exploration of targets for the potential presence of UV fluorescence (cf., Fisk et al., 2015). Early experimentation with the SHERLOC spectrometer indicated a substantial decrease in signal-to-noise ratios after local sunset and during nighttime measurements (Fries et al., 2022).
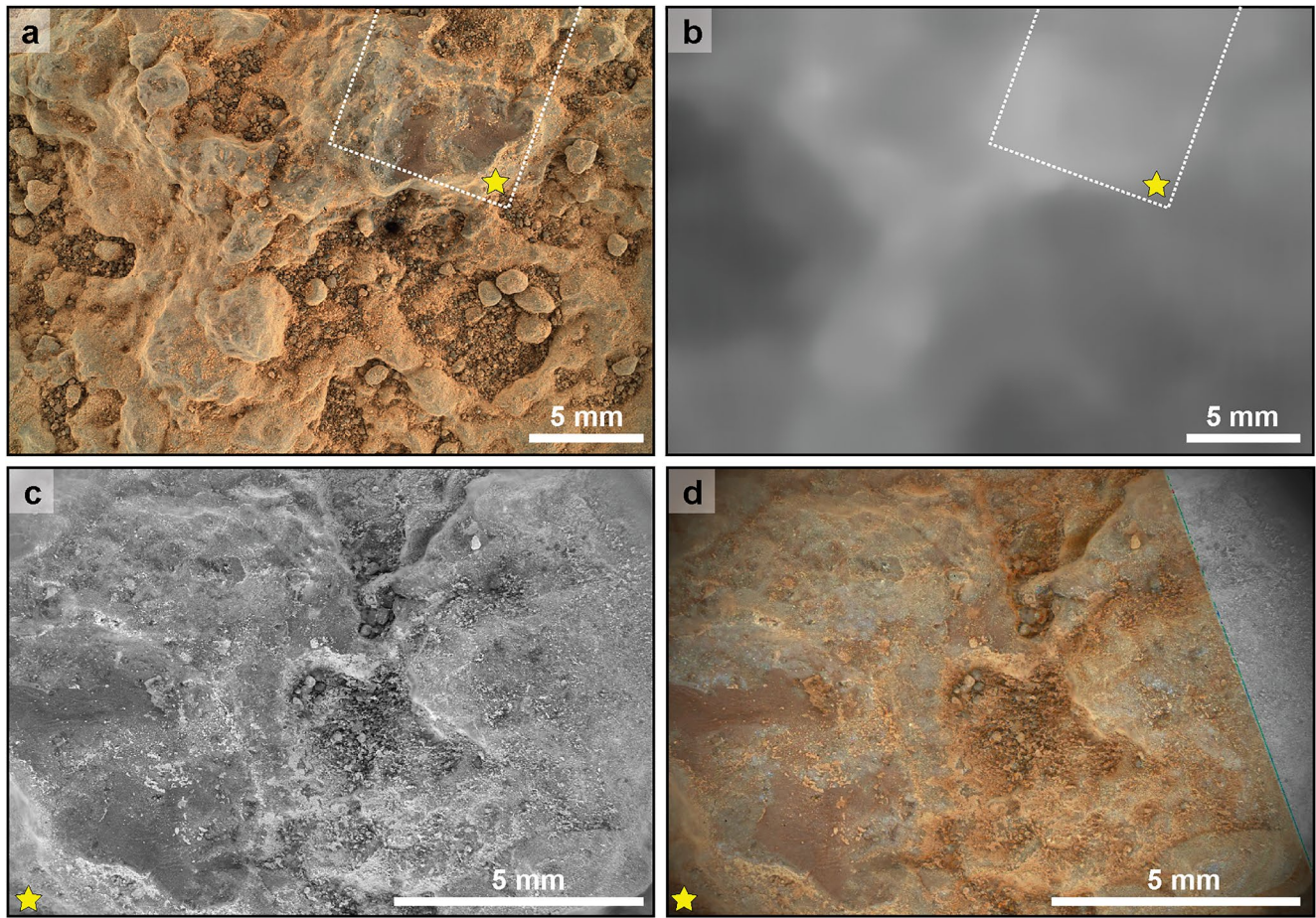
Figure 5. Wide Angle Topographic Sensor for Operations and eNgineering (WATSON) and Autofocus and Contextual Imager (ACI) image products. (a) WATSON focus merge product for target Foux, taken from 4 cm working distance. Dotted white polygon represents the portion of the WATSON image colocated with the ACI image product, and the yellow star is in the same location on all images. Image SI1_0140_0679334136_035FDR_N0051812SRLC00003_000095J05. (b) Topographic relief of the Foux target is highlighted in the range map, in which the palest pixels represent best-focus at 39.3 ± 1 mm focal distance, and the darkest pixels represent best-focus at 45.4 ± 1 mm focal distance. (c) ACI focus merge product for target Foux. (d) Colorized image product using both WATSON and ACI images. Incomplete overlap of WATSON and ACI images led to the observed partial colorization.

Therefore, the majority of ACI images, which are used to focus the spectrometer laser and provide context for spectral observations, are also acquired at night using both groups of white LEDs.

3.2. Image Products

Once WATSON or ACI images have been acquired for a focus stack, they can be merged onboard the rover or manually on Earth to create best-focus full-color images and grayscale range maps (Figure 5). Range maps utilize the dynamic focus range of pixels to provide a representation of the physical relief of the surface (Figure 5b). Range maps can be used to assess placement of proximity instruments such as the abrasion tool and PIXL. Image mosaics are stitched together on the ground after image downlink. WATSON images are also used to colorize grayscale ACI images (Figure 5d).

Colorization of ACI images uses a custom Python script that registers the corresponding focus merged and flat-fielded ACI image with focus merged WATSON images to create an overlay. Keypoint detection is then performed using the Binary Robust Invariant Scalable Keypoints (BRISK) method and descriptors are subsequently matched using the Fast Library for Approximate Nearest Neighbors (FLANN)-based matcher within the OpenCV python package (Bradski, 2000; Leutenegger et al., 2011). Colors from the two images are then blended in hue, saturation, and value space to create a colorized ACI. Although small artifacts of the colorization process are visible in some images as brightly colored spots, the combination of multiple working distance images,

stereo images, focus merged products, and colorized ACI images provide a microscale understanding of surface topography, texture, and dust coverage, providing a robust contextualization of proximity science activities (cf., Corpolongo et al., 2023; Scheller et al., 2022).

4. WATSON as an Engineering Tool

4.1. Instrument Commission Phase

After landing, the first 100 sols included commissioning and checkout of the Perseverance rover instruments, ensuring that all instruments were in good health after cruise and landing. The commissioning phase, referred to as SOX (Surface Operations Transition), consisted of activities critical to nominal surface operations. Initial activities were focused on transitioning the Perseverance rover from its flight software, deploying the mast, and performing instrument aliveness checks; during this time, the first WATSON (e.g., Figure 3a) and ACI images were taken with the arm stowed. The second stage of activities focused on commissioning the robotic arm, checkout of the sample handling assembly, deployment of the Ingenuity helicopter, and continued instrument calibration.

As an arm-mounted camera, WATSON played a critical role during the second phase of SOX. Upon deployment of the robotic arm, WATSON was used to characterize thermally induced drift of the arm. This was achieved by positioning WATSON perpendicular to the bit carousel dock at a 15 cm stand-off distance and acquiring WATSON images—with white LEDs on—periodically over a 24 hr period. The thermal drift was calculated from the positional coordinates of docking features in each image (Figure 6b) using the pixel scale, working distance, and the temperature measured by arm-mounted thermal sensor.

WATSON was also used to inspect rover hardware and verify the deployment of mechanisms that are either underneath the rover or in positions on the rover that are not readily visible to the mast instruments (e.g., SHERLOC and PIXL calibration targets). During flight, instruments housed on the rover underbelly (e.g., the Sampling and Caching Subsystem and the Ingenuity helicopter) were protected by shielding. WATSON was used to ascertain successful firing of the pyrotechnic devices for shielding release as well as device inspection. Release of the Ingenuity helicopter (Balaram et al., 2021) from its flight storage beneath the rover was a particularly complex process that included releasing the protective shielding, swinging the helicopter down from its flight position, deploying the helicopter legs, and releasing the blades. The robotic arm positioned WATSON to image each step in the 10-day staged deployment process, with ground-in-the-loop between firing of each pyrotechnic device to confirm success of each deployment stage (Figure 6).

4.2. Enabling Proximity Science, Abrasion, and Coring

Because WATSON is arm-mounted and can accurately determine its position (and by extension that of the arm) via the focus motor count-working distance relationship, it is a critical tool for proximity science instrument placement, abrasion, and core acquisition. End-to-end robotic arm positioning accuracy is a function of both the absolute positioning accuracy of the robotic arm and the accuracy of stereo imaging. Arm positioning accuracy is pose-dependent and is affected by a combination of primary manufacturing tolerances, joint sensor accuracy, controller performance, and thermal stability. At the outset, these provide an end-to-end arm placement accuracy on the order of several centimeters—which is large enough to make abrasion and drill core placements inaccurate (Moeller et al., 2021) or prohibit postabrasion placement requirements for the highest quality SHERLOC and PIXL data (Allwood et al., 2020; Bhartia et al., 2021). Positioning accuracy of the robotic arm is improved by specifying the desired target in WATSON images. WATSON images that cover the span of the turret stabilizers (35–40 cm working distance) support stabilizer placement in areas free of topography or debris that might cause slippage of the turret during abrasion or sampling. Range data provided by the focus motor count-working distance relationship and/or range maps reduce arm positional uncertainty to the scale of several millimeters, decreasing the risk during arm, tool, and instrument placement.

The successful acquisition of the first two core samples (Simon et al., 2023) was also assisted by WATSON images. Successful coring requires the rock to be stable during robotic arm placement and rotary percussive coring (Moeller et al., 2021). Upon arrival at the coring target Rochette, the potential for an undercut on the backside of the rock was suggested in the HazCam and NavCam images, raising concerns over instability and
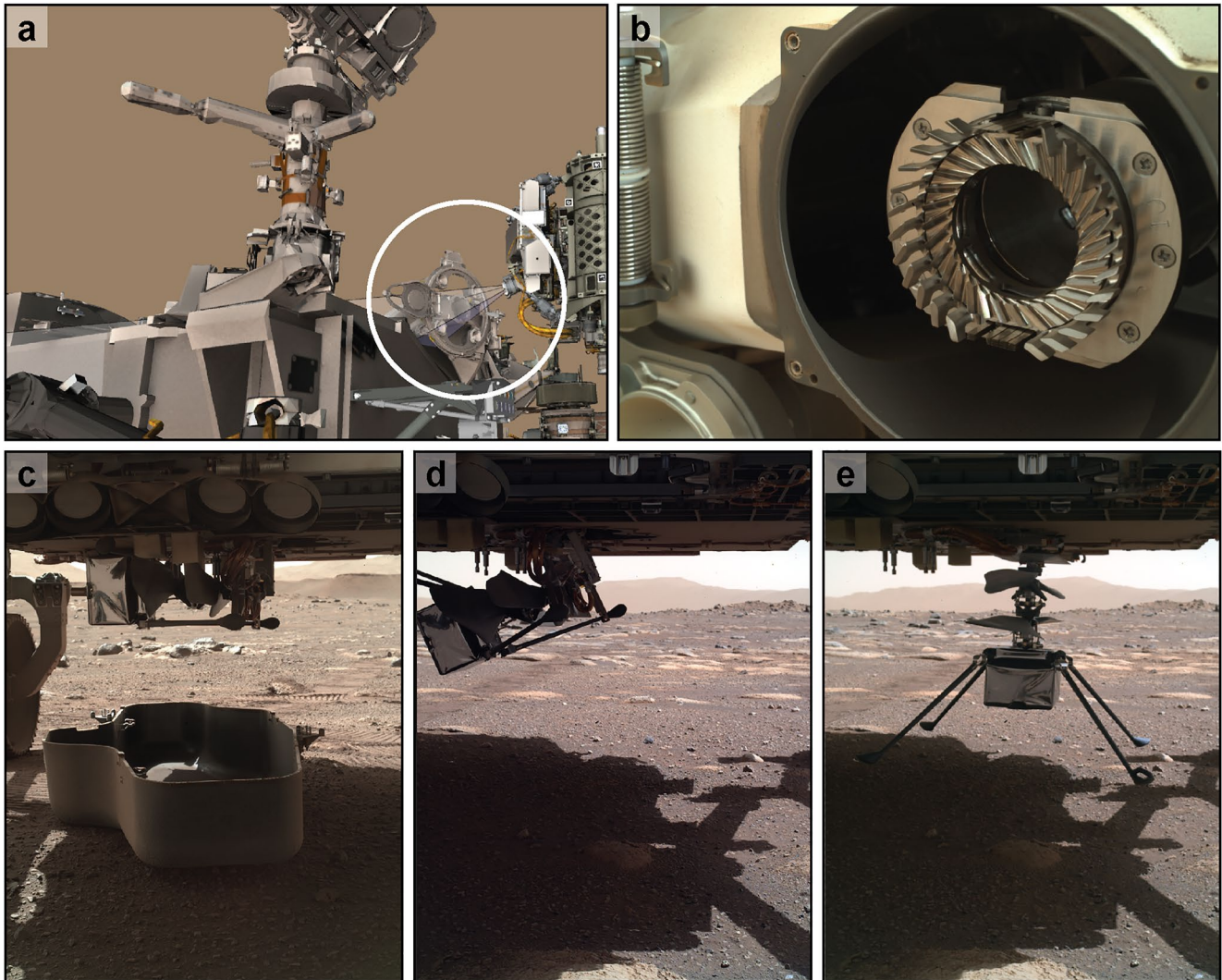
Figure 6. Wide Angle Topographic Sensor for Operations and eNgineering (WATSON) use in instrument deployment. (a) Simulation showing the pointing and imaged location on the rover (white circle) used for assessing the thermal drift of the robotic arm. (b) One of four WATSON images, taken during a 24-hr thermal cycle, to provide landmarks for assessing thermal drift. Image SIF_0076_0673664753_445FDR_N0032430SRLC07018_0000LUJ01. (c) WATSON image showing successful release of shielding that protected the Ingenuity helicopter during flight. Image SIF_0030_0669611931_110FDR_N0030828SRLC07000_0000LUJ01. (d) WATSON image showing partial deployment of the Ingenuity helicopter. Image SIF_0037_0670231583_115FDR_N0031392SRLC07000_0000LUJ01. (e) WATSON image showing successful deployment of the Ingenuity helicopter's legs. Image SIF_0039_0670409192_515FDR_N0031392SRLC07000_0000LUJ01.

rock movement during coring. Perseverance engineers were able to position WATSON to acquire 60 cm stand-off stereo images of the back side of the rock occluded from view of the other rover cameras. Because the baseline for stereo images is well-understood through kinematic modeling of the robotic arm, a stereo mesh could be generated from the WATSON stereo image pair. The WATSON stereo mesh was then superimposed on similar HazCam and NavCam stereo meshes, which showed that Rochette was likely to remain stable during the coring activity.

4.3. Health and Safety of Rover Instruments

During the Crater Floor Campaign, WATSON imaging was also used to diagnose issues related to the Perseverance rover and instrument anomalies. Most critically, during the fourth drill campaign (Quartier target Rlocation, Figure 1c), the coring bit failed to dock properly with the bit carousel during the attempt to transfer the sample to the Sampling and Caching Subsystem (SCS). WATSON was used to image the bit carousel to assess the prob-
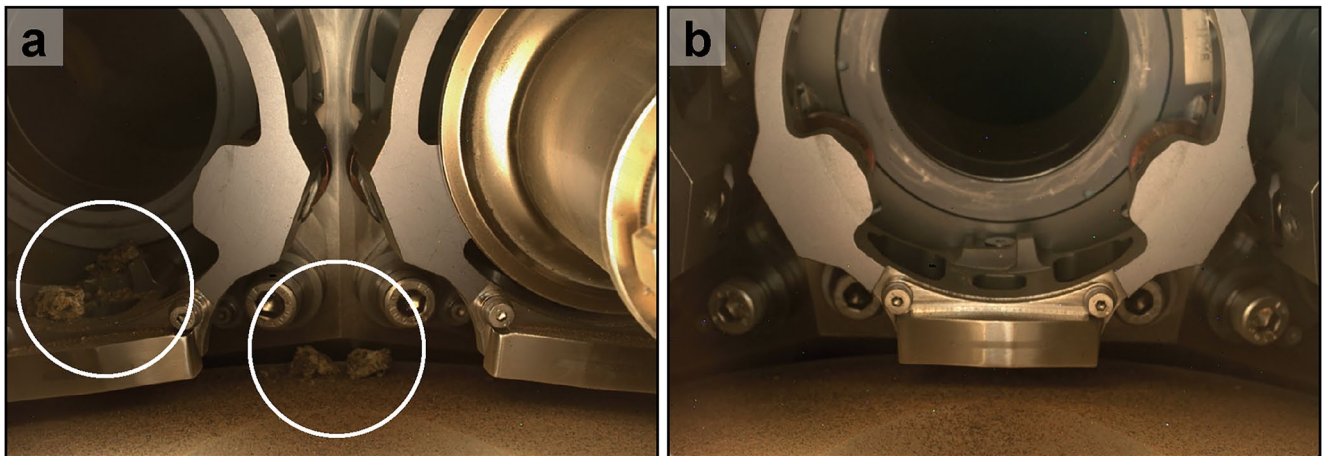
Figure 7. Centimeter-scale rock fragments from a fragmented core (Pauls, Issole locality, Séítah) lodged in the bit carousel during docking of the drill bit. (a) White circles mark fragments both within the bit carousel locking mechanism and between the bit carousel and its housing. Image SIF_0325_0695791198_242FDR_N0090000SRLC07040_0000LMJ01. (b) Postremediation image showing successful dislodging of rock fragments. Image SIF_0332_0696415784_628FDR_N0090082SRLC07041_0000LMJ01.

lem. It was discovered that fractures in the subsurface of the rock—not visible on the surface—had resulted in crumbling of the core, and several pebbles had fallen out of the sample tube during drill bit docking and lodged both within the bit carousel and between the bit carousel and its housing (Figure 7). As a result, rover engineers designed a series of activities that canted the rover into a favorable position for gravity release of the pebbles and assisted release by rotating the bit carousel and using vibrational/percussive activities to dislodge the pebbles. WATSON was used to image the bit carousel after each stage, and to acquire a video of the bit carousel rotation to ascertain that these efforts resulted in unrestricted movement of the carousel.

During this same time interval, it had become apparent that MEDA (Rodriguez-Manfredi et al., 2021) began showing anomalies related to a variety of sensor failures. WATSON imaging was undertaken to diagnose the potential for physical damage (i.e., breaking of 30 μm sensor leads) using a total of 17 camera positions. Ultimately, it was determined that the wind sensor dies were likely damaged from the kinetic energy of pebble transport during high wind conditions. This diagnosis permitted the MEDA team to redesign the wind measurement protocol to utilize the remaining undamaged and partially damaged dies.

5. WATSON and ACI Observations of Geologic Targets

5.1. Natural Surfaces

After commissioning of the rover was completed, the science team began exploring the origins of the crater floor materials, including the Máaz formation, the underlying Séítah formation, and surficial regolith materials. Prior to the first abrasion activity, all WATSON imaging was performed on unmodified outcrop surfaces, termed natural surfaces by the mission. After abrasion activities were commissioned (Farley et al., 2022), natural surface observations have been generally restricted to images used for understanding rock stability or to identify and assess potential abrasion and sampling targets (see Table S1).

Natural surfaces have proven to be difficult to interpret even when using the highest-resolution WATSON images. Nearly all observed natural surfaces show some combination of extensive mechanical weathering (i.e., crumbling), wind abrasion (i.e., fluting and polishing), and the presence of coatings (cf., Clavé et al., 2022; Farley et al., 2022; Herkenhoff et al., 2023). During early parts of the Crater Floor Campaign, targeting was focused on examining low-lying, polygonal "paver" stones that were common in the landing region. The texture of these rocks, which were typically only a few centimeters above the regolith surface, were often obscured with a combination of dust, and two distinct size fractions of regolith, fine-grained and coarse-grained (cf.,

Horgan et al., 2023; Vaughan et al., 2023). Distinct size fractions are common in Martian regolith (cf., Minitti et al., 2014; Sullivan et al., 2005). Multiple of the Máaz pavers show a knobby surface that is on a similar scale to the mm-sized, coarse-grained, regolith particles (Figures 8a and 8b) however, geochemical evidence suggests that the coarse-grained regolith fraction is dominated by Séítah-sourced olivine grains (Vaughan et al., 2023).

Fluting by wind abrasion is also a commonly observed phenomenon in WATSON images of natural surfaces in Jezero crater (Figure 8). Although fluting is observed in some targets at only a few centimeters above the regolith surface, it is more common on rocks that are >10 cm above the regolith surface. Fluting provides a strong lineation to the rock surface that obscures textures, such as bedding or jointing, that reflect the primary rock lithology. On higher-standing rocks, which tend to be more dust-free, fluting is also associated with polishing of the rock surface that reflects sunlight and can obscure visibility of surface details. Dust-free surfaces also commonly reveal a continuous to patchy dark red to purple coating. Such coatings are exciting in that they indicate the potential evidence of chemical alteration in contact with the martian atmosphere or fluids (cf., Clavé et al., 2022; Farley et al., 2022), but they also effectively conceal the underlying primary rock fabric.

5.2. Abraded Surfaces

WATSON and ACI images of crater floor abrasion targets have been more informative than those of natural surfaces (see Table S2). Except for a few targets (e.g., Figure 9a), it has been difficult to correlate surface textures between preabrade and postabrade images. During the abrasion process, a rotating abrade bit grinds approximately 8 mm into the rock surface, followed by multiple blasts of compressed gas from the Gas Dust Removal Tool (gDRT) to remove tailings (Moeller et al., 2021). WATSON images of the abrasion patches are typically taken at 25 cm, 7 cm, and 4 cm stand-off to evaluate texture and grain relationships and to support targeting for PIXL and SHERLOC spectroscopy. Here we discuss abrasion patches for Dourbes (Séítah formation, Bastide member), Quartier (Séítah formation, Issole member), Guillaumes (Máaz formation, Roubion member), Bellegarde (Máaz formation, Rochette member), Montpezat (Máaz formation, Artuby member), and Alfalfa (Máaz formation, Ch'ał member). Roubion is the basal member of the Máaz formation and unconformably overlies the Séítah formation in contact with the Issole member (Farley et al., 2022; Horgan et al., 2023; Stack et al., 2020; Sun et al., 2023).

Orbital (Horgan et al., 2020), remote (Wiens et al., 2022), and proximity (Liu et al., 2022) science all indicate a transition from olivine-dominated rocks in the Séítah formation to pyroxene-dominated materials in the Máaz formation (Farley et al., 2022). WATSON and ACI images (Figures 9–11) show that the textures of these materials also vary between the two formations. Rocks of the Séítah formation consist of predominantly angular to subrounded monocrystalline olivine and minor pyroxene, with an Fe-silicate matrix (Liu et al., 2022), and carbonate and sulfate detections predominantly at olivine crystal margins (Scheller et al., 2021). WATSON (Figures 9a and 9b) and ACI (Figures 10a and 10b) images clearly show individual olivine and pyroxene crystals. Colorized ACI images (Figures 11a and 11b) also highlight both the internal texture of crystal grains, which are generally translucent with opaque regions possibly related to incipient alteration of these ultramafic grains, and alteration rims, which have also been documented in SuperCam Remote Micro-Imager (RMI) images of Séítah rocks (Wiens et al., 2022). These colorized ACI images also show that exposures of Séítah nearest to the overlying Máaz formation, represented by the abrasion target Quartier, contain a higher proportion of late-stage mineralization phases containing sulfate and potentially perchlorate salts (Scheller et al., 2022).

Abrasion patches of Máaz materials (Figures 9c–9e, 9f and 10c–10f) show complex and ambiguous textures consisting of <500 μm dark-toned and light-toned grains; these differ dramatically from the sub-mm to sub-cm scale grains (<0.1–0.4 cm) that are readily observed in Séítah formation rocks. Colorized ACI images of targets Guillaumes and Bellegarde (Figures 11c–11f) contain substantial light-toned material associated with late diagenetic precipitation of sulfate salts (Scheller et al., 2022; Tice et al., 2022). Within the Guillaumes target, however, these light-toned phases appear to occur throughout the rock, suggesting fluid movement along fractures and grain boundaries, whereas in the Bellegarde target these phases are restricted to irregularly shaped pores. WATSON and ACI images of the Montpezat and Alfalfa abrade targets (Figures 9e and 9f and
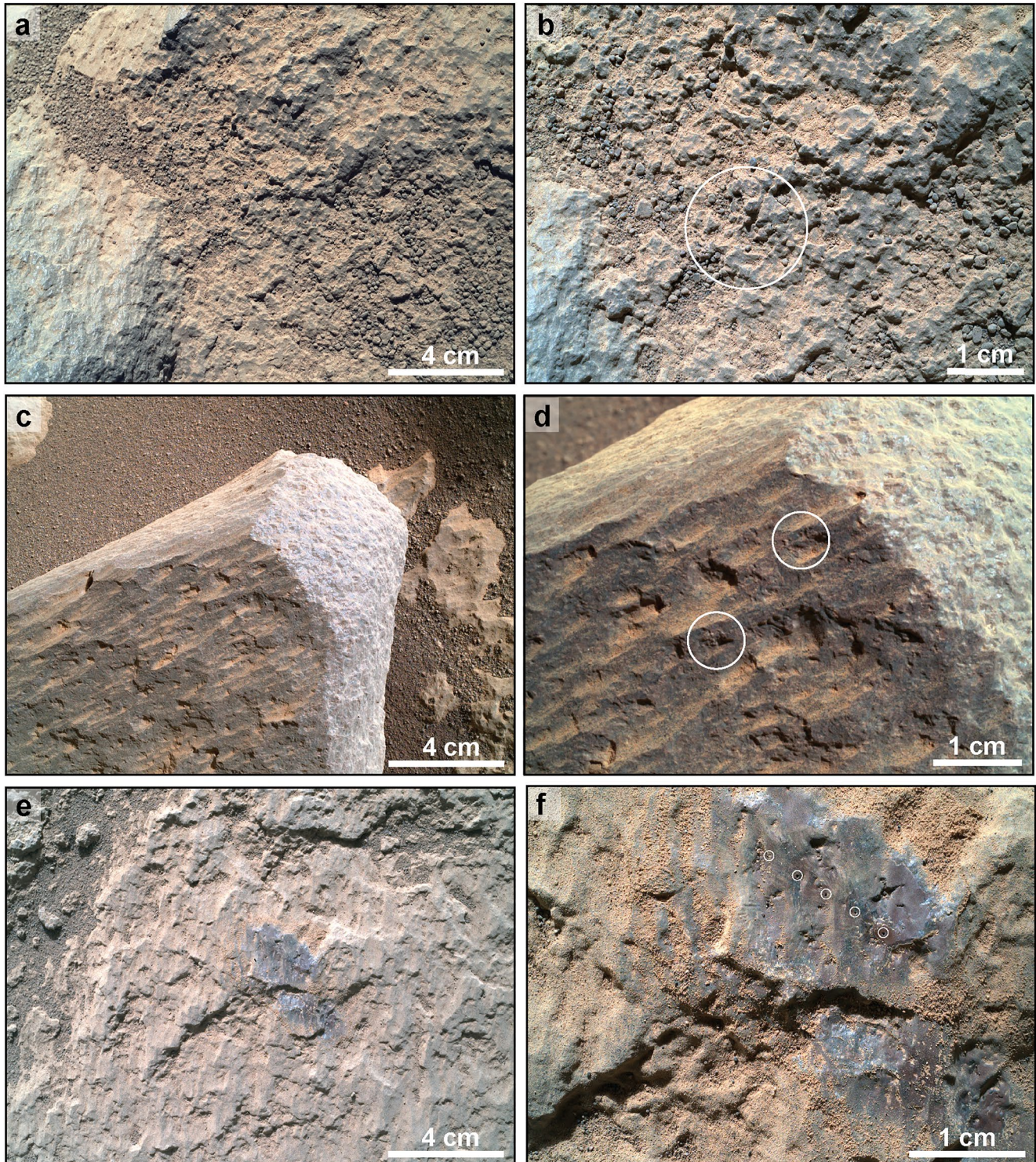
Figure 8.

Figures 10e and 10f) record sub-mm-scale light and dark-toned grains similar to those seen in Guillaumes. By contrast to the Guillaumes and Bellegarde samples (Figures 9d and 9c and 10c and 10d), which show Fe-oxide staining associated with potential primary voids, Fe-oxide staining in the Montpezat and Alfalfa targets is more sparse and does not appear to be associated with any specific phase, suggesting that it may be related to fluids that permeated the rock matrix.

5.3. Regolith Targets

In addition to rock targets, WATSON enables characterization of many of the common metrics used to evaluate soil properties on Earth, including grain size, grain shape, degree of sorting, and color of regolith. Additionally, WATSON can be used in conjunction with other techniques, such as SuperCam Laser Induced Breakdown Spectrometry (LIBS; Wiens et al., 2020) and VIS and VISIR spectral imaging (Kinch et al., 2020; Maurice et al., 2021), to generate cross-scale imaging measurements and links between chemistry and mineralogy detections. During the Crater Floor Campaign, the different scales and techniques of inquiry provided by the Perseverance rover instrument suite were utilized to characterize crater floor regolith and to build hypotheses regarding the formation mechanisms of the potential regolith classes observed throughout the mission (cf. Cousin et al., 2022; Vaughan et al., 2023).

Deployment of WATSON on dedicated regolith targets was limited during the Crater Floor Campaign, and neither SHERLOC nor ACI were deployed on a dedicated regolith target. Nonetheless, regolith on and around bedrock targets commonly occurs in WATSON images (see Table S3). WATSON imaging captured three primary regolith types: fine-grained regolith, coarse-grained regolith, and mixed regolith (Figure 12). The mixed regolith is characterized by angular to subrounded pebble-sized rock fragments that resemble local bedrock. Mixed regolith occurs most commonly at the immediate perimeter of bedrock outcrops and float blocks, and the texture, color, and mineralogy of pebble-sized clasts changes with local outcrop composition (Vaughan et al., 2023). As such, mixed regolith is considered to be highly locally derived. Mixed regolith also covers much of the inter-outcrop terrain in the Máaz and Séítah formations, suggesting the potential to identify lithologies that are buried beneath regolith.

Coarse and fine grains regolith types observed in Jezero are similar to regolith previously reported by landed missions elsewhere on Mars (Minitti et al., 2014; Sullivan et al., 2005; Weitz et al., 2018; Yingst et al., 2013; Yingst, Cropper, et al., 2016; Yingst, Edgett, et al., 2016). Coarse-grained regolith consists of subangular to well-rounded gray grains with long axes between 1 and 2 mm. Coarse-grained regolith occurs across a variety of settings, including accumulated on low-standing outcrops (e.g., Figure 8a), unevenly scattered among other regolith types (Figure 12b), and armoring aeolian bedforms. Olivine was detected by multispectral observations from Mastcam-Z and SuperCam VISIR (e.g., Beyssac et al., 2021; Mandon et al., 2022 LPSC; Vaughan et al., 2021) and by chemical measurements from SuperCam LIBS (Beyssac et al., 2021) in coarse-grained regolith, regardless of the location of the regolith (i.e., Máaz or Séítah). The lack of olivine in Máaz bedrock (Farley et al., 2022; Horgan et al., 2020, 2023; Liu et al., 2022) strongly links the source of the olivine-bearing coarse-grained regolith to Séítah bedrock (Vaughan et al., 2023). The ubiquitous presence of coarse-grained regolith and the general roundedness of the grains indicate they have been transported throughout the Crater Floor Campaign area. Their larger grain size, however, suggests movement by an impact creep process (Minitti et al., 2014; Sullivan et al., 2005).

By contrast, fine-grained regolith consists predominantly of very fine to medium sand (80–530 mm on the Wentworth scale). Grains are typically multicolored, and include distinct red, black, gray, white, and translucent grains, often showing slight variation in overall hue in regions directly adjacent to outcrops. Such multicolored regolith is similar to that observed elsewhere on Mars and likely represents mixing and homogenization of aeolian-transported materials that derive from rocks exposed over broad regions of the Martian surface. Variation in color adjacent to local outcrops may reflect either an increase in grain contribution from local outcrops, or perhaps shielding of adjacent regolith from atmospheric dust accumulation. Atmospheric dust is the fine-grained element of the regolith. Although individual dust particles cannot be resolved in WATSON images, clumps of dust are commonly visible on rock surfaces (e.g., Figure 8f).

Figure 8. Wide Angle Topographic Sensor for Operations and eNgineering (WATSON) images of natural rock surfaces of the Máaz formation. (a, b) The tsé'éwózítah (lots of pebbles) target at 25 and 12 cm stand-off distances. Ground-level exposures are oftentimes heavily covered by dust and have a knobby surface which could potentially source the observed mm-scale grains (b, circle). Images SIF_0071_0673253362_500FDR_N0032208SRLC02500_0000LUJ01 and SIF_0071_0673253477_363FDR_N0032208SRLC01260_0000LUJ01. (c, d) Higher-standing rocks, such as the ahíłhane' (conversation) target, here at 25 and 9 cm stand-off distances, often show fluting that can be attributed to long-term abrasion by wind. Individual grains are not visible except potentially at the edges of certain flutes (d, circles). Images SIF_0082_0674237852_468FDR_N0032430SRLC02536_0000LUJ01 and SI1_0082_0674240824_753ECZ_N0032430SRLC00003_000095J01. (e, f) Strongly fluted surface of the naat'áanii (leadership) target; laser shots from Supercam LIBS analyses (f, circles) successfully removed dust to reveal a reddish-purple coating that covers patches of the eroded rock surface. Images SIF_0078_0673880527_574FDR_N0032430SRLC02500_0000LUJ01 and SIF_0078_0673880658_343FDR_N0032430SRLC00660_0000LUJ01.
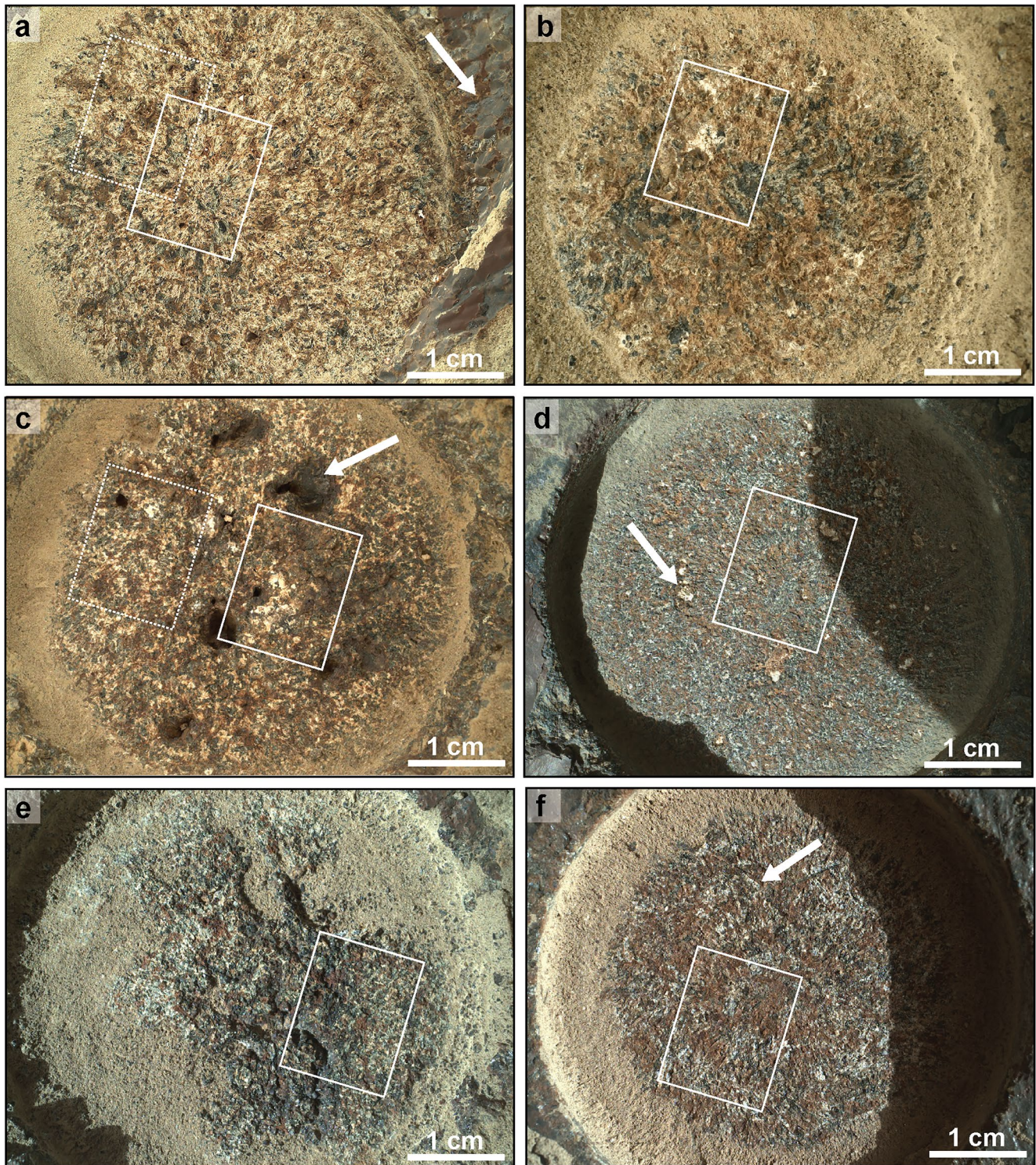
Figure 9.

6. Discussion

Imaging is at the heart of a significant amount of operational and scientific decisions that take place during the strategic and tactical time frames of a rover mission. WATSON images of natural and abraded surfaces provide detailed, distinct, and contrasting views of rock targets. Although intrinsic rock textures on natural surfaces are typically obscured by a combination of atmospheric dust, aeolian abrasion, and coatings, particularly within

the Máaz formation, WATSON images of abraded patches have been instrumental in guiding geological and petrological interpretations of the Jezero crater floor rocks.

The coarse-grained nature of the Séítah formation was discernible in limited regions of WATSON imaging of natural surfaces, but not to the same extent to which it was visible in SuperCam RMI images (cf. Kah et al., 2022; Wiens et al., 2022). One factor that might explain this discrepancy is the orientation of images. Although WATSON is capable of taking images at a variety of orientations, the dominant use of WATSON on natural surfaces is to support abrasion and core acquisition operations. This results in WATSON being used primarily on the upper surface of outcrops, which may experience a different erosional regime. Future WATSON imaging on the side of outcrops may be able to provide more details about intrinsic rock texture.

By contrast, combined WATSON and ACI images on abrasion patches have proven quite fruitful in terms of providing key textural analysis and context for core acquisition. Abrasion targets within the Séítah formation illustrate key relationships between grains, alteration rims, matrix components, and the precipitation of diagenetic salts. The Séítah formation has been interpreted as an ultramafic, olivine-bearing cumulate that is potentially related to the olivine-bearing unit outside of Jezero crater (Beyssac et al., 2023; Corpolongo et al., 2023; Liu et al., 2022). Textures observed in WATSON and ACI images, particularly when colocated with SHERLOC spectroscopy and PIXL investigations (e.g., Schmidt et al., 2022), have provided critical observations for the development of the cumulate hypothesis (Liu et al., 2022). Detailed analysis of these fabrics can be used to place constraints on emplacement mechanism hypotheses. Although interpretation of abrasion targets within the overlying Máaz formation is more complex, WATSON and ACI images support a multistage emplacement of the Máaz formation in which the basal portions may show greater textural heterogeneity than the upper portions of the formation. Additionally, WATSON and ACI images show a distinct array of secondary precipitation phases (cf. Scheller et al., 2022). These secondary salts may be concentrated in the interval that spans the interface between the Séítah and Máaz formations as they are present in the lowest Máaz (Guillaumes) and the adjacent Seitah (Quartier) targets. However, similar salts are also observed within primary voids of the Bellegarde target but are rare in Montpezat, which sits stratigraphically between Guillaumes and Bellegarde. The timing of precipitation of these salt phases is not yet known, however; their occurrence may represent either penetration of lacustrine waters into underlying lithologies during deposition of the Máaz formation, or later-diagenetic fluid flow that was concentrated at lithologic boundaries.

7. Conclusions

Turret-mounted imaging systems, WATSON and ACI, play a vital role in the Mars 2020 mission for both science and engineering. During the earliest stages of the mission, WATSON imaging was critical to the successful commissioning of the Perseverance rover, its instrument payload, and the Ingenuity helicopter. WATSON remains an important tool for assessment of engineering activities that enable the successful abrasion, coring, and caching of rock samples. During the Crater Floor Campaign data gleaned from natural surface WATSON images was limited, in contrast to the vital textures observed within the abraded patches. Continued use of WATSON on natural surfaces and abrasion targets will facilitate textural interpretations of deltaic facies in addition to bridging the "resolution gap" between Mastcam-Z/NavCam and ACI images.

Figure 9. Wide Angle Topographic Sensor for Operations and eNgineering (WATSON) images of abraded targets at 7 cm stand-off; broadly radial lineations are marks from the abrade bit. Solid white rectangles show localization of Autofocus and Contextual Imager (ACI) images documented in this figure; dotted white rectangles are ACI images shown below in Figure 10. (a) Dourbes abrasion patch, Séítah formation, contains mm-scale gray grains visible on the unabraded surface (arrow) are tan (olivine) and green-gray (pyroxene) on the abraded surface. Image number: SI1_0269_0690819279_328ECZ_N0080000SRLC00062_000095J01. (b) Quartier abrasion, Séítah formation, contains mm-scale grains similar to those in Dourbes, but shows more red-brown coloration resulting from Fe-oxidative weathering and white patches associated with secondary mineral precipitates. Image number: SI1_0292_0692866773_550ECM_N0090000SRLC00702_0000LMJ01. (c) Guillaumes target, lower Máaz formation, contains smaller grains, dark brown partial voids (e.g., arrow), and abundant white patches associated with secondary minerals. Image number: SI1_0160_0681180536_921ECZ_N0060000SRLC00003_000095J01. (d) Bellegarde abrasion, Máaz formation, records a generally fine texture with abundant, irregularly shaped voids filled with secondary mineral precipitates (arrow). Image number: SI1_0185_0683375452_164ECZ_N0070000SRLC00001_000095J01. (e, f) Montpezat (Image number: SI1_0346_0697668598_804ECZ_N0092982SRLC00033_000095J01) and Alfalfa (Image number: SI1_0367_0699533528_843ECZ_ N0110108SRLC00033_000095J01) abrasion targets, Máaz formation, show homogeneous distribution of sometimes elongate (arrow) pale and dark grains and red-brown staining associated with Fe-oxidative weathering.
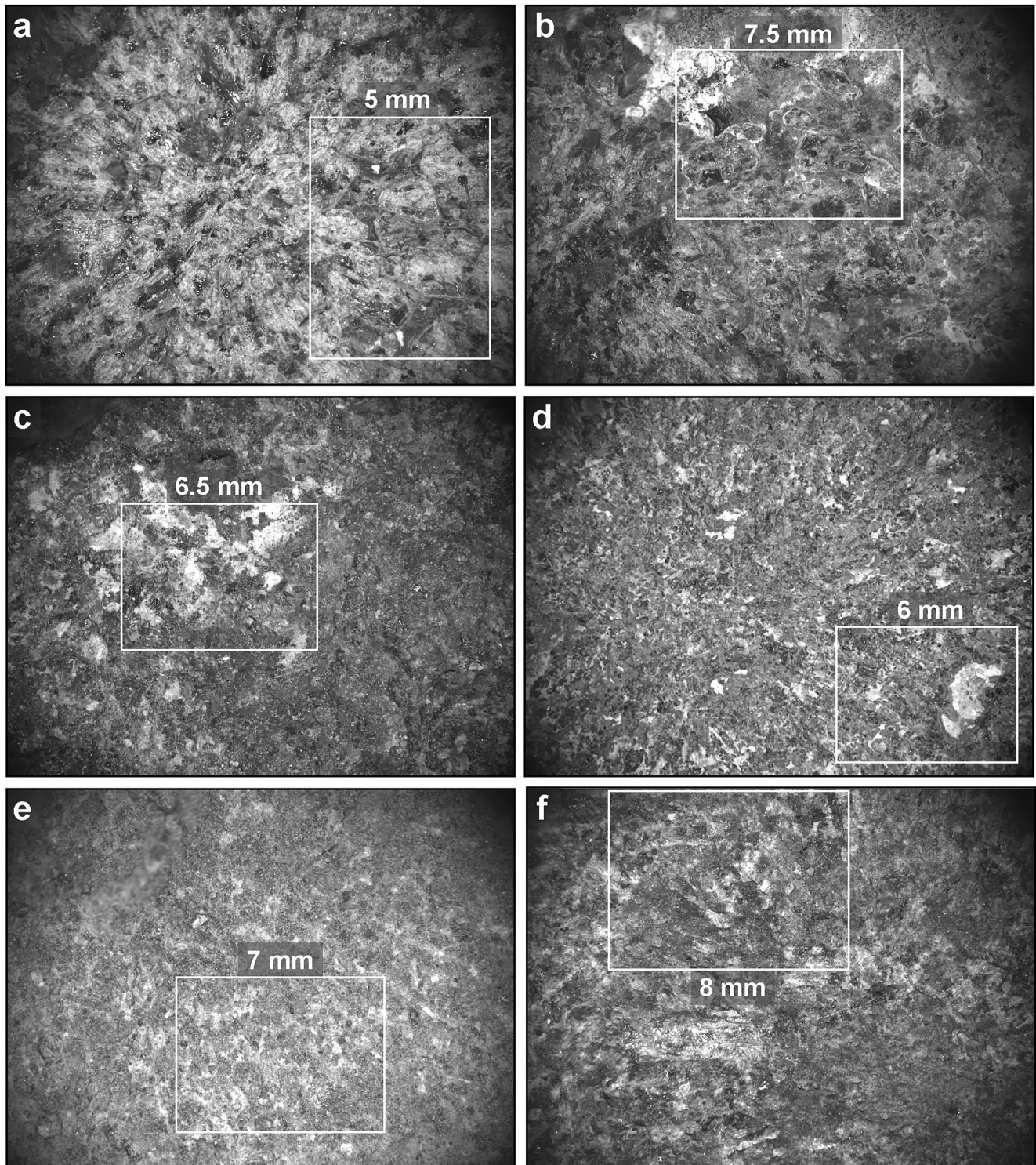
Figure 10. Autofocus and Contextual Imager (ACI) images of abrasion targets; broadly radial lineations are marks from the abrade bit. Solid white rectangles show regions detailed with colorized ACI images in Figure 11 and serve as individualized scale bars. Targets Dourbes (a) and Quartier (b) of the Séítah formation are clearly more coarsely grained than any of the Máaz formation samples (c)–(f). Images SC3_0257_0689786372_972FDR_N0080000SRLC11421_0000LUJ01 and SC3_0293_0692982194_468FDR_N0090000SRLC10300_0000LMJ01. Target Guillaumes (c) of the lowermost Máaz formation, like Quartier (b), which is preserved directly below the Máaz contact, both record substantial precipitation of secondary phases (white in image) throughout the rock matrix. Target Bellegarde (d) similarly contains precipitation of secondary phases, but these phases are largely restricted to primary pores in the rock matrix. Image SC3_0186_0683479674_054FDR_N0070000SRLC11420_0000LMJ02. Targets Montpezat (e) and Alfalfa (f) are distinctly more homogeneous across the abrade regions and do not show clear precipitation of light-toned, secondary minerals. Images SC3_0349_0697951235_031FDR_N0092982SRLC11360_0000LMJ01 and SC3_0370_0699816329_039FDR_N0110108SRLC10600_0000LMJ01.
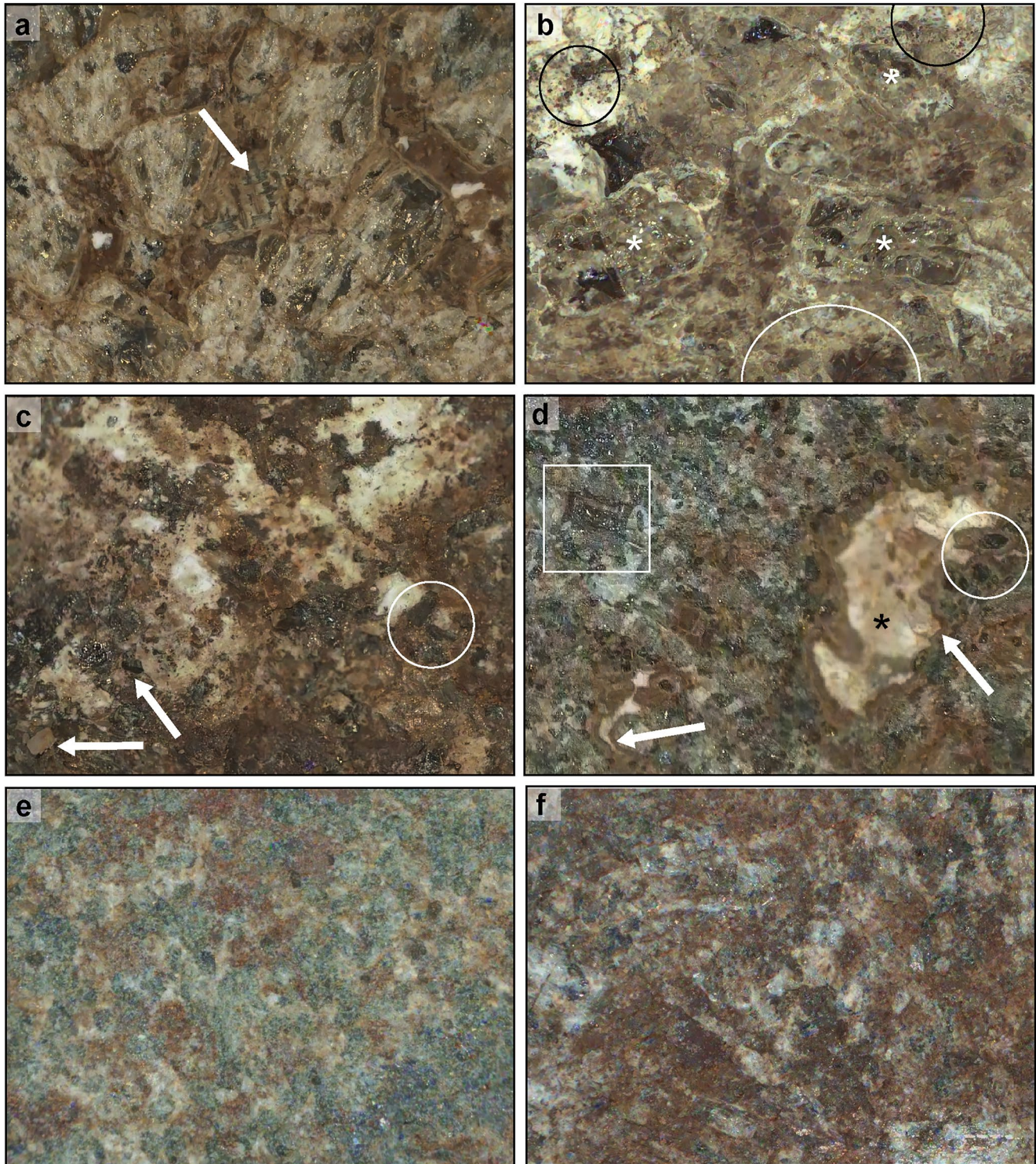
Figure 11. Details of abrasion targets in colorized Autofocus and Contextual Imager (ACI) images. Long/Horizontal axis of all images is 10 mm. (a) Dourbes image showing the translucent nature of beige-colored olivine grains; more opaque regions likely reflect incipient alteration. Olivine crystals also show distinct, layered alteration rims. Cross-hatched structure of a single grain (arrow) suggests possible orthopyroxene with both cleavage and exsolution layering. Matrix component is dominantly opaque brown, with small patches of light-toned secondary minerals. (b) Quartier retains 1.0–2.5 mm olivine crystals (asterisks), with light-toned phases rimming the boundaries. Opaque, approximately 0.1 mm brown granules (black circles) and 0.25–1.0 mm rounded grains (white circle) are commonly associated with light-toned mineral phases. (c) Guillaumes target contains abundant secondary light-toned phases. 500 µm-scale dark-toned grains (white circle) and several surficial grains (arrows) are also noted. (d) Bellegarde target shows a complex texture that includes possible skeletal olivine (white square), and irregularly shaped primary voids lined with dark-toned crystals (white circle), an isopachous Mg-sulfate phase (arrows), and a late-stage Ca-sulfate void filling phase (asterisk). Other Máaz formation targets Montpezat (e) and Alfalfa (f) show regionally homogeneous texture; note that Fe-oxide staining does not appear to have an association with any single mineral phase.
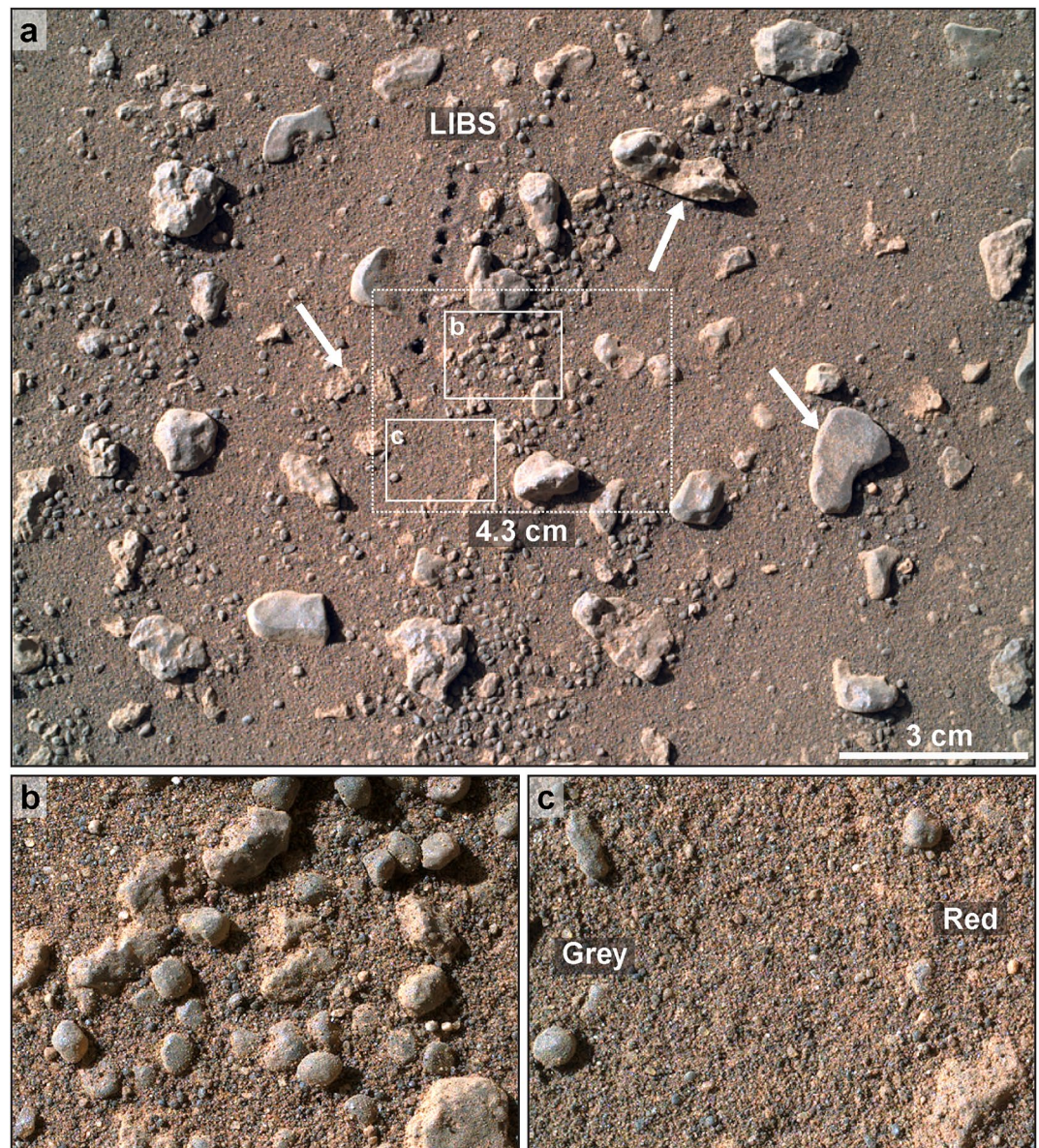
Figure 12. Regolith varieties of the Jezero crater floor. (a) Regolith target kwe'é (right here) imaged at 25 cm stand-off, showing three main regolith types and a series of pits from SuperCam LIBS analyses. Arrows denote centimeter-scale pebbles that are similar in color and texture to local outcrop of the Máaz formation. Image SIF_0115_0677161052_339FDR_ N0041062SRLC02503_0000LUJ01. Dotted rectangle shows coverage of Wide Angle Topographic Sensor for Operations and eNgineering (WATSON) from a 6 cm stand-off; Image SI1_0115_0677163779_875FDR_N0041062SRLC00054_000090J01. Solid rectangles mark localities of images (b, c). (b) Mixed regolith pebbles with a sparse contribution of rounded grains that characterize coarse-grained regolith. (c) Variously colored grains that characterize fine-grained regolith; note local variation in color from gray to red, which may indicate variation in contribution from airfall dust (cf. Vaughan et al., 2023).

Data Availability Statement

The mission data used for collating WATSON and ACI images in the study are available as supplementary data tables and at Open Science Framework (OSF) repository via https://doi.org/10.17605/OSF.IO/W36V2 without an account under CC-By Attribution 4.0 International (Wogsland, 2023).

References

Allwood, A. C., Wade, L. A., Foote, M. C., Elam, W. T., Hurowitz, J. A., Battel, S., et al. (2020). Pixl: Planetary instrument for X-ray lithochemistry. *Space Science Reviews*, *216*(8), 1–132. https://doi.org/10.1007/s11214-020-00767-7

Andrews-Hanna, J. C., & Lewis, K. W. (2011). Early Mars hydrology: 2. Hydrological evolution in the Noachian and Hesperian epochs. *Journal of Geophysical Research*, *116*(E2), E02007. https://doi.org/10.1029/2010JE003709

Balaram, J., Aung, M., & Golombek, M. P. (2021). The ingenuity helicopter on the Perseverance rover. *Space Science Reviews*, *217*(4), 56. https://doi.org/10.1007/s11214-021-00815-w

Beyssac, O., Forni, O., Cousin, A., Udry, A., Kah, L. C., Mandon, L., et al. (2023). Petrological traverse of an olivine-pyroxene cumulate on the floor of Jezero Crater, Mars: A perspective from SuperCam onboard Perseverance. *Journal of Geophysical Research: Planets*, *128*, e2022JE007638. https://doi.org/10.1029/2022JE007638

Beyssac, O., Gasnault, O., Chide, B., Clave, E., Cousin, A., Forni, O., et al. (2021). Mafic chemistry and mineralogy (including olivine) of the coarse-grained regolith analyzed by SuperCam at Jezero Crater, Mars (Abstract P25A-08). *Paper presented at 2021 American Geophysical Union Fall Meeting, San Francisco, CA*.

Bhartia, R., Beegle, L. W., DeFlores, L., Abbey, W., Razzell Hollis, J., Uckert, K., et al. (2021). Perseverance's scanning habitable environments with Raman and luminescence for organics and chemicals (SHERLOC) investigation. *Space Science Reviews*, *217*(4), 58. https://doi.org/10.1007/s11214-021-00812-z

Bradski, G. (2000). The OpenCV library [software]. *Journal of Software Tools*, *120*, 122–125. Retrieved from https://opencv.org/

Bramble, M. S., Mustard, J. F., & Salvatore, M. R. (2017). The geological history of Northeast Syrtis major, Mars. *Icarus*, *293*, 66–93. https://doi.org/10.1016/j.icarus.2017.03.030

Brown, A. J., Hook, S. J., Baldridge, A. M., Crowley, J. K., Bridges, N. T., Thomson, B. J., et al. (2010). Hydrothermal formation of clay-carbonate alteration assemblages in the Nili Fossae region of Mars. *Earth and Planetary Science Letters*, *297*(1–2), 174–182. https://doi.org/10.1016/J.EPSL.2010.06.018

Brown, A. J., Viviano, C., & Goudge, T. A. (2020). Olivine-carbonate mineralogy of the Jezero crater region. *Journal of Geophysical Research: Planets*, *125*(3), e2019JE006011. https://doi.org/10.1029/2019JE006011

Carr, M. H., & Head, III, J. W. (2003). Oceans on Mars: An assessment of the observational evidence and possible fate. *Journal of Geophysical Research*, *108*(E5), 5042. https://doi.org/10.1029/2002JE001963

Clavé, E., Benzerara, K., Meslin, P.-Y., Forni, O., Royer, C., Mandon, L., et al. (2022). Carbonate detection with SuperCam in igneous rocks on the floor of Jezero Crater, Mars. *Journal of Geophysical Research: Planets*, *127*(6), e2022JE007463. https://doi.org/10.1029/2022JE007463

Corpolongo, A., Jakubek, R. S., Burton, A. S., Brown, A. J., Yanchilina, A., Czaja, A. D., et al. (2023). SHERLOC Raman mineral class detections of the Mars 2020 Crater Floor campaign. *Journal of Geophysical Research: Planets*, *128*(3), e2022JE007455. https://doi.org/10.1029/2022JE007455

Cousin, A., Meslin, P. Y., Hausrath, E. M., Cardarelli, E., Lasue, J., Beyssac, O., et al. (2022). Soil diversity at Mars: Comparison of dataset from gale and Jezero craters (Contribution No. 2678). In *Paper presented at 53rd Lunar and Planetary Science Conference, Woodlands, TX, USA*.

Crumpler, L. S., Horgan, B., Simon, J., Stack, K., Alwmark, S., Gilles, D., et al. (2023). In situ geologic context mapping transect on the floor of Jezero Crater from Mars 2020 Perseverance rover observations. *Journal of Geophysical Research: Planets*, *128*, e2022JE007444. https://doi.org/10.1029/2022JE007444

Davis, J. M., Balme, M., Grindrod, P. M., Williams, R. M. E., & Gupta, S. (2016). Extensive Noachian fluvial systems in Arabia Terra: Implications for early Martian climate. *Geology*, *44*(10), 847–850. https://doi.org/10.1130/G38247.1

Edgett, K. S. (2021). Perseverance's SHERLOC WATSON—Post-landing refinement of relations between focus, range, and image scale using images acquired on Mars, plus an update on particulates on the detector. *Zenodo*. https://doi.org/10.5281/zenodo.5555292

Edgett, K. S., Caplinger, M. A., Maki, J. N., Ravine, M. A., Ghaemi, F. T., McNair, S., et al. (2015). *Curiosity's robotic arm-mounted Mars Hand lens imager (MAHLI): Characterization and calibration status, MSL MAHLI (Technical Report 0001, version 2)*. Mars Science Laboratory. https://doi.org/10.13140/RG.2.1.3798.5447

Edgett, K. S., Caplinger, M. A., & Ravine, M. A. (2019). *Mars 2020 Perseverance SHERLOC WATSON camera pre-delivery characterization and calibration report*. Malin Space Science Systems. https://doi.org/10.13140/RG.2.2.18447.00165

Edgett, K. S., & Sarkar, R. (2021). Recognition of sedimentary rock occurrences in satellite and aerial images of other worlds—Insights from Mars. *Remote Sensing*, *13*(21), 4296. https://doi.org/10.3390/rs13214296

Edgett, K. S., Yingst, R. A., Ravine, M. A., Caplinger, M. A., Maki, J. N., Ghaemi, F. T., et al. (2012). Curiosity's Mars Hand lens imager (MAHLI) investigation. *Space Science Reviews*, *170*(1–4), 259–317. https://doi.org/10.1007/s11214-012-9910-4

Ehlmann, B. L., Mustard, J. F., Swayze, G. A., Clark, R. N., Bishop, J. L., Poulet, F., et al. (2009). Identification of hydrated silicate minerals on Mars using MRO-CRISM: Geologic context near Nili Fossae and implications for aqueous alteration. *Journal of Geophysical Research*, *114*, E00D08. https://doi.org/10.1029/2009JE003339

Farley, K. A., Stack, K. M., Horgan, B. H. N., Tarnas, J., Sun, V. Z., Shuster, D. L., et al. (2022). Aqueously altered igneous rocks on the floor of Jezero crater, Mars. *Science*, *377*, 6614. https://doi.org/10.1126/science.abo2196

Farley, K. A., Williford, K. H., Stack, K. M., Bhartia, R., Chen, A., de la Torre, M., et al. (2020). Mars 2020 mission overview. *Space Science Reviews*, *216*(8), 142. https://doi.org/10.1007/s11214-020-00762-y

Fassett, C. I., & Head, J. W. (2005). Fluvial sedimentary deposits on Mars: Ancient deltas in a crater lake in the Nili Fossae region. *Geophysical Research Letters*, *32*, L14201. https://doi.org/10.1029/2005GL023456

Fisk, M., Pommerenck, J., Watkins-Brandt, K., Edgett, K., Minitti, M., Hardgrove, C., et al. (2015). UV-excited fluorescence of rocks in Gale crater, Mars (Abstract P51E-07). *Presented at presented at 2015 American Geophysical Union Fall Meeting, San Francisco, CA*.

Fries, M. D., Lee, C., Bhartia, R., Razzell Hollis, J., Uckert, K., Beegle, L. W., et al. (2022). The SHERLOC calibration target on the Mars 2020 Perseverance rover: Design, operations, outreach, and future human exploration functions. *Space Science Reviews*, *218*(6), 46. https://doi.org/10.1007/s11214-022-00907-1

Garvin, J. B., Edgett, K. S., Dotson, R., Fey, D. M., Herkenhoff, K. E., Hallet, B. J., & Kennedy, M. R. (2017). Quantitative relief models of rock surfaces on Mars at sub-millimeter scales from Mars Curiosity rover Mars Hand Lens Imager (MAHLI) observations: Geologic implications. *Microscopy and Microanalysis*, *23*(S1), 2146–2147. https://doi.org/10.1017/S1431927617011394

Goudge, T. A., Mustard, J. F., Head, J. W., Fassett, C. I., & Wiseman, S. M. (2015). Assessing the mineralogy of the watershed and fan deposits of the Jezero crater paleolake system, Mars. *Journal of Geophysical Research: Planets*, *120*, 775–808. https://doi.org/10.1002/2014JE004782

Grotzinger, J. P., Sumner, D. Y., Kah, L. C., Stack, K., Gupta, S., Edgar, L., et al. (2014). A habitable fluvio-lacustrine environment at Yellowknife Bay, Gale crater, Mars. *Science*, *343*(6169), 1242777. https://doi.org/10.1126/science.1242777

Herkenhoff, K. E., Sullivan, R. J., Newman, C. E., Paar, G., Baker, M., Viúdez-Moreiras, D., et al. (2023). Comparison of ventifact orientations and recent wind direction indicators on the floor of Jezero Crater, Mars. *Journal of Geophysical Research: Planets*, *128*(3), e2022JE007599. https://doi.org/10.1029/2022JE007599

Holm-Alwmark, S., Kinch, K. M., Hansen, M. D., Shahrzad, S., Svennevig, K., Abbey, W. J., et al. (2021). Stratigraphic relationships in Jezero Crater, Mars: Constraints on the timing of fluvial-lacustrine activity from orbital observations. *Journal of Geophysical Research: Planets*, *126*(7), e2021JE006840. https://doi.org/10.1029/2021JE006840

Horgan, B. H. N., Rice, M., Udry, A., Holm-Alwmark, S., Amundsen, H. E. F., Bell, J. F., et al. (2023). Mineralogy, morphology, and emplacement history of the Maaz formation on the Jezero crater floor from orbital and rover observations. *Journal of Geophysical Research: Planets*, *128*, e2022JE007612. https://doi.org/10.1029/2022JE007612

Horgan, B. N., Anderson, R. B., Dromart, G., Amador, E. S., & Rice, M. S. (2020). The mineral diversity of Jezero crater: Evidence for possible lacustrine carbonates on Mars. *Icarus*, *339*, 113526. https://doi.org/10.1016/j.icarus.2019.113526

Hundal, C. B., Mustard, J. F., Kremer, C. H., Tarnas, J. D., & Pascuzzo, A. C. (2022). The Circum-Isidis Capping Unit: An extensive regional Ashfall deposit exposed in Jezero Crater. *Geophysical Research Letters*, *49*(9), e2021GL096920. https://doi.org/10.1029/2021GL096920

Kah, L. C., Minitti, M., Cardarelli, E., Mangold, N., Liu, Y., Gupta, S., et al. (2022). Use of size frequency distributions in the interpretation of planetary surface materials (Contribution No. 2678). *Paper presented at 53rd Lunar and Planetary Science Conference, Woodlands, TX, USA.*

Kah, L. C., Stack, K. M., Eigenbrode, J. L., Yingst, R. A., & Edgett, K. S. (2018). Syndepositional precipitation of calcium sulfate in Gale Crater, Mars. *Terra Nova*, *30*(6), 431–439. https://doi.org/10.1111/ter.12359

Kinch, K. M., Madsen, M. B., Bell, J. F., Maki, J. N., Bailey, Z. J., Hayes, A. G., et al. (2020). Radiometric calibration targets for the Mastcam-Z camera on the Mars 2020 rover mission. *Space Science Reviews*, *216*(8), 1–51. https://doi.org/10.1007/s11214-020-00774-8

Kminek, G., Meyer, M. A., Beaty, D. W., Carrier, B. L., Haltigin, T., & Hays, L. E. (2022). Mars Sample Return (MSR): Planning for returned sample science. *Astrobiology*, *22*(S1), S-1–S-4. https://doi.org/10.1089/AST.2021.0198

Kremer, C. H., Mustard, J. F., & Bramble, M. S. (2019). A widespread olivine-rich ash deposit on Mars. *Geology*, *47*(7), 677–681. https://doi.org/10.1130/G45563.1

Leutenegger, S., Chli, M., & Siegwart, R. Y. (2011). BRISK: Binary Robust invariant scalable keypoints. In *2011 international conference on computer vision.* https://doi.org/10.1109/iccv.2011.6126542

Liu, Y., Tice, M. M., Schmidt, M. E., Treiman, A. H., Kisovski, T. V., Hurowitz, J. A., et al. (2022). An olivine cumulate outcrop on the floor of Jezero crater, Mars. *Science*, *377*(6614), 1513–1519. https://doi.org/10.1126/science.abo2756

Malin, M. C., & Edgett, K. S. (2003). Evidence for persistent flow and aqueous sedimentation on early Mars. *Science*, *302*(5652), 1931–1934. https://doi.org/10.1126/science.1090544

Mandon, L., Quantin-Nataf, C., Royer, C., Beck, O., Fouchet, T., & Johnson, J. R. (2022). Infrared reflectance of rocks and regolith at Jezero Crater: One Year of SuperCam observations (Contribution No. 2678). *Paper presented at 53rd Lunar and Planetary Science Conference, Woodlands, TX, USA.*

Mandon, L., Quantin-Nataf, C., Thollot, P., Mangold, N., Lozac'h, L., Dromart, G., et al. (2020). Refining the age, emplacement and alteration scenarios of the olivine-rich unit in the Nili Fossae region, Mars. *Icarus*, *336*, 113436. https://doi.org/10.1016/j.icarus.2019.113436

Mangold, N., Dromart, G., Ansan, V., Salese, F., Kleinhans, M. G., Massé, M., et al. (2020). Fluvial regimes, morphometry, and age of Jezero Crater paleolake inlet valleys and their exobiological significance for the 2020 rover mission landing site. *Astrobiology*, *20*(8), 994–1013. https://doi.org/10.1089/ast.2019.2132

Mangold, N., Gupta, S., Gasnault, O., Dromart, G., Tarnas, J. D., Sholes, S. F., et al. (2021). Perseverance rover reveals an ancient delta-lake system and flood deposits at Jezero crater, Mars. *Science*, *374*(6568), 711–717. https://doi.org/10.1126/science.abl4051

Mangold, N., Poulet, F., Mustard, J. F., Bibring, J. P., Gondet, B., Langevin, Y., et al. (2007). Mineralogy of the Nili Fossae region with OMEGA/Mars express data: 2. Aqueous alteration of the crust. *Journal of Geophysical Research*, *112*(E8), E08S04. https://doi.org/10.1029/2006JE002835

Maurice, S., Wiens, R. C., Bernardi, P., Caïs, P., Robinson, S., Nelson, T., et al. (2021). The SuperCam instrument suite on the Mars 2020 rover: Science Objectives and mast-unit description. *Space Science Reviews*, *217*(3), 1–108. https://doi.org/10.1007/s11214-021-00807-w

Minitti, M. E., Edgett, K. S., Yingst, R. A., Conrad, P. G., Fisk, M., Hardgrove, C. J., et al. (2014). MAHLI after dark: Nighttime Mars Hand lens imager observations under LED illumination (Contribution No. 1777, Abstract 2029). *Paper presented at Lunar and Planetary Institute, Houston, TX, USA* (Vol. 45).

Minitti, M. E., Kah, L. C., Yingst, R. A., Edgett, K. S., Anderson, R. C., Beegle, L. W., et al. (2013). MAHLI at the Rocknest sand shadow: Science and science-enabling activities. *Journal of Geophysical Research: Planets*, *118*, 2338–2360. https://doi.org/10.1002/2013JE004426

Moeller, R. C., Jandura, L., Rosette, K., Robinson, M., Samuels, J., Silverman, M., et al. (2021). The sampling and caching Subsystem (SCS) for the scientific exploration of Jezero Crater by the Mars 2020 Perseverance rover. *Space Science Reviews*, *217*(1), 1–43. https://doi.org/10.1007/s11214-020-00783-7

Murchie, S. L., Mustard, J. F., Ehlmann, B. L., Milliken, R. E., Bishop, J. L., McKeown, N. K., et al. (2009). A synthesis of Martian aqueous mineralogy after 1 Mars year of observations from the Mars Reconnaissance Orbiter. *Journal of Geophysical Research*, *114*, E00D06. https://doi.org/10.1029/2009JE003342

Mustard, J. F., Ehlmann, B. L., Murchie, S. L., Poulet, F., Mangold, N., Head, J. W., et al. (2009). Composition, morphology, and stratigraphy of Noachian crust around the Isidis basin. *Journal of Geophysical Research*, *114*, E00D12. https://doi.org/10.1029/2009JE003349

Mustard, J. F., Poulet, F., Head, J. W., Mangold, N., Bibring, J. P., Pelkey, S. M., et al. (2007). Mineralogy of the Nili Fossae region with OMEGA/Mars express data: 1. Ancient impact melt in the Isidis Basin and implications for the transition from the Noachian to Hesperian. *Journal of Geophysical Research*, *112*(E8), E08S03. https://doi.org/10.1029/2006JE002834

Perron, J. T., Mitrovica, J. X., Manga, M., Matsuyama, I., & Richards, M. A. (2007). Evidence for an ancient Martian ocean in the topography of deformed shorelines. *Nature*, *447*(7146), 840–843. https://doi.org/10.1038/nature05873

Rice, M. S., Johnson, J. R., Million, C. C., St. Clair, M., Horgan, B. N., Vaughan, A., et al. (2023). Spectral variability of rocks and soils on the Jezero crater floor: A summary of multispectral observations from Perseverance's Mastcam-Z instrument. *Journal of Geophysical Research: Planets*, *128*, e2022JE007548. https://doi.org/10.1029/2022JE007548

Rodriguez-Manfredi, J. A., de la Torre Juárez, M., Alonso, A., Apéstigue, V., Arruego, I., Atienza, T., et al. (2021). The Mars environmental dynamics analyzer, MEDA. A suite of environmental sensors for the Mars 2020 mission. *Space Science Reviews*, *217*(3), 1–86. https://doi.org/10.1007/S11214-021-00816-9

Salese, F., McMahon, W. J., Balme, M. R., Ansan, V., Davis, J. M., & Kleinhans, M. G. (2020). Sustained fluvial deposition recorded in Mars' Noachian stratigraphic record. *Nature Communications*, *11*(1), 2067. https://doi.org/10.1038/s41467-020-15622-0

Salese, F., Pondrelli, M., Neeseman, A., Schmidt, G., & Ori, G. G. (2019). Geological evidence of planet-wide groundwater system on Mars. *Journal of Geophysical Research: Planets*, *124*(2), 374–395. https://doi.org/10.1029/2018JE005802

Scheller, E. L., & Ehlmann, B. L. (2020). Composition, stratigraphy, and geological history of the Noachian Basement surrounding the Isidis impact basin. *Journal of Geophysical Research: Planets*, *125*, e2019JE006190. https://doi.org/10.1029/2019JE006190

Scheller, E. L., Razzell Hollis, J., Cardarelli, E. L., Steele, A., Beegle, L. W., Bhartia, R., et al. (2022). Aqueous alteration processes and implications for organic geochemistry in Jezero crater, Mars. *Science*, *378*(6624), 1105–1110. https://doi.org/10.1126/science.abo5204

Scheller, E. L., Swindle, C., Grotzinger, J., Barnhart, H., Bhattacharjee, S., Ehlmann, B. L., et al. (2021). Formation of Magnesium carbonates on Earth and implications for Mars. *Journal of Geophysical Research: Planets*, *126*(7), e2021JE006828. https://doi.org/10.1029/2021JE006828

Schmidt, M. E., Allwood, A., Christian, J., Clark, B. C., Flannery, D., Hennecke, J., et al. (2022). Highly differentiated lavas examined by the PIXL instrument in Jezero crater (Contribution No. 1530). *Paper presented at 53rd Lunar and Planetary Science Conference, Woodlands, TX, USA*.

Shahrzad, S., Kinch, K. M., Goudge, T. A., Fassett, C. I., Needham, D. H., Quantin-Nataf, C., & Knudsen, C. P. (2019). Crater statistics on the dark-toned, mafic floor Unit in Jezero Crater, Mars. *Geophysical Research Letters*, *46*, 2408–2416. https://doi.org/10.1029/2018GL081402

Sharma, S., Roppel, R. D., Murphy, A., Beegle, L. W., Bhartia, R., Steele, A., et al. (2023). Diverse organic-mineral associations in Jezero crater, Mars. *Nature*, *619*(7971), 724–732. https://doi.org/10.1038/S41586-023-06143-Z

Simon, J. I., Hickman-Lewis, K., Cohen, B. A., Mayhew, L. E., Shuster, D. L., Debaille, V., et al. (2023). Samples collected from the floor of Jezero Crater with the Mars 2020 Perseverance rover. *Journal of Geophysical Research: Planets*, *128*(6), e2022JE007474. https://doi.org/10.1029/2022JE007474

Stack, K. M., Williams, N. R., Calef, F., Sun, V. Z., Williford, K. H., Farley, K. A., et al. (2020). Photogeologic map of the Perseverance rover field site in Jezero Crater Constructed by the Mars 2020 science team. *Space Science Reviews*, *216*(127), 127. https://doi.org/10.1007/s11214-020-00739-x

Sullivan, R., Banfield, D., Bell, J. F., Calvin, W., Fike, D., Golombek, M., et al. (2005). Aeolian processes at the Mars exploration rover Meridiani Planum landing site. *Nature*, *436*(7047), 58–61. https://doi.org/10.1038/nature03641

Sun, V. Z., Hand, K. P., Stack, K. M., Farley, K. A., Milkovich, S., Kronyak, R., et al. (2023). Exploring the Jezero Crater Floor: Overview of results from the Mars 2020 Perseverance rover's first science campaign. *Journal of Geophysical Research: Planets*, *128*. https://doi.org/10.1029/2022JE007613

Sun, V. Z., & Stack, K. M. (2020). Geologic map of Jezero crater and the Nili Planum region, Mars. *U.S. Geological Survey Scientific Investigations Map 3464, Pamphlet 14 p., 1 Sheet, Scale 1:75,000*. https://doi.org/10.3133/sim3464

Tarnas, J. D., Mustard, J. F., Lin, H., Goudge, T. A., Amador, E. S., Bramble, M. S., et al. (2019). Orbital identification of hydrated silica in Jezero Crater, Mars. *Geophysical Research Letters*, *46*(22), 12771–12782. https://doi.org/10.1029/2019GL085584

Tarnas, J. D., Stack, K. M., Parente, M., Koeppel, A. H. D., Mustard, J. F., Moore, K. R., et al. (2021). Characteristics, origins, and biosignature preservation potential of carbonate-bearing rocks within and outside of Jezero crater. *Journal of Geophysical Research: Planets*, *126*(11), e2021JE006898. https://doi.org/10.1029/2021JE006898

Tice, M. M., Hurowitz, J. A., Allwood, A. C., Jones, M. W. M., Orenstein, B. J., Davidoff, S., et al. (2022). Alteration history of Seitah formation rocks inferred by PIXL X-ray flourescences, X-ray diffraction, and multispectral imaging on Mars. *Science Advances*, *8*, 47. https://doi.org/10.1126/sciadv.abp9084

Vaughan, A., Minitti, M. E., Cardarelli, E. L., Johnson, J. R., Kah, L. C., Pilleri, P., et al. (2023). Regolith of the crater floor units, Jezero crater, Mars: Textures, composition, and implications for provenance. *Journal of Geophysical Research: Planets*, *128*(3), e2022JE007437. https://doi.org/10.1029/2022JE007437

Vaughan, A., Rice, M. S., Horgan, B. H. N., Johnson, J. R., Bell, J. F., Núñez, J. I., et al. (2021). A Mastcam-Z view of regolith at Jezero Crater: Textural and spectral properties (Poster P251). *Paper presented at American Geophysical Union Fall Meeting, New Orleans, LA, USA*.

Viviano, C. E., Moersch, J. E., & McSween, H. Y. (2013). Implications for early hydrothermal environments on Mars through the spectral evidence for carbonation and chloritization reactions in the Nili Fossae region. *Journal of Geophysical Research: Planets*, *118*(9), 1858–1872. https://doi.org/10.1002/jgre.20141

Weitz, C. M., Sullivan, R. J., Lapotre, M. G. A., Rowland, S. K., Grant, J. A., Baker, M., & Yingst, R. A. (2018). Sand grain sizes and shapes in Eolian Bedforms at gale crater, Mars. *Geophysical Research Letters*, *45*(18), 9471–9479. https://doi.org/10.1029/2018GL078972

Wiens, R. C., Udry, A., Beyssace, O., Quantin-Nataf, C., Mangold, N., Cousin, A., et al. (2022). Compositionally and density stratified igneous terrain in Jezero Crater, Mars. *Science Advances*, *8*, 34. https://doi.org/10.1126/sciadv.abo3399

Wiens, R. C., Wan, X., Lasue, J., & Maurice, S. (2020). Laser-induced breakdown spectroscopy in planetary science. In *Laser-induced breakdown spectroscopy* (pp. 441–471). https://doi.org/10.1016/b978-0-12-818829-3.00020-4

Williams, R. M. E., Grotzinger, J. P., Dietrich, W. E., Gupta, S., Sumner, D. Y., Wiens, R. C., et al. (2013). Martian fluvial conglomerates at gale crater. *Science*, *340*(6136), 1068–1072. https://doi.org/10.1126/science.1237317

Williford, K. H., Farley, K. A., Stack, K. M., Allwood, A. C., Beaty, D., Beegle, L. W., et al. (2018). The NASA Mars 2020 rover mission and the search for extraterrestrial life. In *From habitability to life on Mars* (pp. 275–308). https://doi.org/10.1016/b978-0-12-809935-3.00010-4

Wogsland, B. V. (2023). Science and science-enabling activities of the SHERLOC and WATSON imaging systems in Jezero Crater, Mars [Dataset]. Open Science Framework (OSF). https://doi.org/10.17605/OSF.IO/W36V2

Yingst, R. A., Cropper, K., Gupta, S., Kah, L. C., Williams, R. M. E., Blank, J., et al. (2016). Characteristics of pebble and cobble-sized clasts along the Curiosity rover traverse from sol 100 to 750: Terrain types, potential sources, and transport mechanisms. *Icarus*, *280*, 72–92. https://doi.org/10.1016/j.icarus.2016.03.001

Yingst, R. A., Edgett, K. S., Kennedy, M. R., Krezoski, G. M., McBride, M. J., Minitti, M. E., et al. (2016). MAHLI on Mars: Lessons learned operating a geoscience camera on a landed payload robotic arm. *Geoscientific Instrumentation, Methods and Data Systems*, *5*(1), 205–217. https://doi.org/10.5194/gi-5-205-2016

Yingst, R. A., Kah, L. C., Palucis, M., Williams, R. M. E., Garvin, J., Bridges, J. C., et al. (2013). Characteristics of pebble- and cobble-sized clasts along the curiosity rover traverse from Bradbury landing to Rocknest. *Journal of Geophysical Research: Planets*, *118*(11), 2361–2380. https://doi.org/10.1002/2013JE004435

Zastrow, A. M., & Glotch, T. D. (2021). Distinct carbonate lithologies in Jezero Crater, Mars. *Geophysical Research Letters*, *48*(9), e2020GL092365. https://doi.org/10.1029/2020GL092365